

NATIONAL RADIO ASTRONOMY OBSERVATORY *

INTERNAL REPORT

RADIO TESTS OF THE NRAO 140-FOOT TELESCOPE
IN THE WAVELENGTH RANGE
BETWEEN 11 and 0.95 CM

P. G. Mezger, H. Brown, I. Pauliny-Toth,
J. Schraml and Z. Turlo

August 1966

*Operated by Associated Universities, Inc., under contract with
the National Science Foundation.

PREFACE

After about one year of observing with and testing of the NRAO 140-foot telescope, we have come to the following conclusions:

- i) The quality of observations in the short cm wavelength range is very closely correlated with the detailed knowledge of the characteristics of the telescope.
- ii) In addition to the gravitational deflections of large reflectors, temperature effects impose a very severe limitation on the observing accuracy of cm-wave telescopes.
- iii) Meteorological conditions impose--through sky noise fluctuations and possibly radio scintillation -- a limitation on the accuracy of radio astronomical observations in the cm-wavelength range which has not been encountered in the longer wavelength range.

Although we are well aware of the fact that our observational experience as well as our test results are far from yielding conclusive results, we have decided to collect all available information pertaining to the characteristics of the 140-foot telescope in the following report. The principal goal of this report is to provide us with a guide for future radio tests and to collect quantitative test results in order to detect possible changes of the telescope characteristics with time.

Colleagues working in a similar field of telescope testing and colleagues who have used the NRAO 140-foot telescope for observations have asked us for copies of this report. After some deliberation we decided to comply

with their requests. But we want to make it clear that this report is a working report with all its disadvantages: insufficient measurements, premature conclusions, etc. We intend to continue the testing of the 140-foot telescope and to collect the results of future tests in supplementary reports.

The results of antenna tolerance theory and of the theory of microwave scintillation, as well as the technique of radio tests of antenna characteristics, are widely discussed in the literature. These subjects are often treated in internal reports which might be difficult to obtain. That is the reason that we have included short reviews on these subjects in this report.



P. G. Mezger

TABLE OF CONTENTS

	Page
I. INTRODUCTION	
a. Short History of Observations and Radiometers	6
b. Some Structural Features of the 140-foot Telescope which are Related with its Radio Frequency Characteristics	8
c. Measuring Techniques	12
II. RANDOM AND LARGE SCALE REFLECTOR DEVIATIONS	
a. Short Review of Antenna Tolerance Theory	22
b. Measurements of Aperture and Beam Efficiency at Various Wavelengths. Determination of the RMS Reflector Deviation and the Aperture Efficiency with Telescope Position	30
c. Variation of Aperture and Beam Efficiency with Telescope Position	
d. Variation of Focal Length with Telescope Position	31
e. Variation of Aperture and Beam Efficiency and Antenna HPBW with Axial Focus Position	32
f. Misalignment of the Rotation Axis of the Sterling Mount with Respect to the Electrical Axis of the 140-foot Reflector	33
g. Determination of Error Pattern and Correlation Length	36

h. Variation of Beam Shape with Telescope Position; Large Scale Reflector Deviations	40
III. POINTING ERRORS	
a. Comparison of Pointing Corrections at Various Wavelengths	43
b. Remaining Pointing Error after Correction for Atmospheric Refraction	44
c. Short Term Pointing Errors	44
d. Daily Pointing Errors	44
e. Correlation Between Pointing Errors and Rotation of Sterling Mount	45
IV. TIME VARYING EFFECTS	
a. Time Variation of Pointing	46
b. Time Variation of Focal Length	46
c. Time Variation of Aperture Efficiency	47
V. INFLUENCE OF ATMOSPHERE	47
a. Short Review of Microwave Scintillation Theory	48
b. Discussion of Methods to Detect Atmospheric Phase Fluctuations	55
c. Observations and Data Reduction	59
d. Interpretation of Observational Results	62
e. Conclusions	65
REFERENCES	68
CAPTIONS	70

RADIO TESTS OF THE NRAO 140-FOOT TELESCOPE IN THE WAVELENGTH RANGE
BETWEEN 11 and 0.95 CM

P. G. Mezger, H. Brown, I. Pauliny-Toth,
J. Schraml and Z. Turlo

I. INTRODUCTION

The NRAO 140-foot telescope was built as a precision instrument for observations in the cm wavelength range. Since the construction is very massive, it was anticipated that the characteristics of this telescope should not change with time or meteorological conditions.

The telescope was put into operation at the end of June 1965 at a wavelength of 6 cm. We found that the indicated focal length of the telescope changed and that the gain decreased with increasing zenith distance. This behavior is typical of all NRAO telescopes whose panels have been adjusted with the telescope pointing towards zenith.

It was only when we started observations at $\lambda = 1.95$ cm with a radiometer of high sensitivity that we noticed that the characteristics of the 140-foot telescope change with time. An apparent correlation between ambient temperature and focal length was found. It was also found that at this short wavelength the characteristics of the 140-foot telescope deteriorate so rapidly with increasing zenith distance that the value of 2-cm observations at low declinations becomes doubtful.

In order to investigate these effects in more detail, one week at the end of the 2 cm observations was spent entirely for telescope tests. It was decided to devote two more weeks in the fall of 1966 to continue these tests.

In this report we try to collect all data available to date on the 140-foot telescope. ~~Based on this data we will outline in the last section of this report a testing program for the forthcoming testing period.~~

I.a. Short History of Observations and Radiometers

The measurements mentioned in this report refer mostly to the short-wave observations performed with the telescope. We compile in the following Table 1 the observing periods and the radiometer parameters of these short-wave observations.

Table 1

	Observing period		ν center GHz	Bandwidth MHz	Radio- meter	Noise Temperature °K	Observer
	Start	End					
I	7-8-65	9-1-65	5.01	8	PA	450	NRAO
II	9-2-65	9-27-65	2.695	10	PA	400	NRAO
III	9-28-65	10-4-65	15.3	12	Mi	2000	NRAO
IV	11-30-65	12-27-65	15	?	Mi	?	NRL
V	12-27-65	1-10-66	31.4	100	Mi	6000	NRAO
VI	1-11-66	2-14-66	5.0	300	TD	700	NRAO
VII	2-14-66	4-4-66	15.3	2000	TD	1200	NRAO
VIII	4-4-66	4-15-66	20	?	Mi	?	NRL
IX	4-15-66	4-29-66	3	?	Mi	?	MIT

To characterize the radiometers used during the various observing periods, we use

Mi = Mixer input

TD = Tunnel diode preamplifier

Pa = Parametric preamplifier

Observations and results in the following are designated by, e.g., "OPV", which stands for "observations made during observing period V, which lasted from December 27, 1965 to January 10, 1966. A mixer input radiometer with a center frequency of 31.4 GHz, a bandwidth of 100 MHz and a single channel noise temperature of 6000 °K was used for these observations."

I. b. Some Structural Features of the 140-foot Telescope which are Related with Its Radio Frequency Characteristics

The 140-foot telescope is polar mounted. Reflector and backup structure are made of aluminum; the remainder of the telescope is made of steel. The total weight of the movable parts of the telescope is 2770 tons. The whole structure is painted with a white, highly and diffusely reflecting paint in order to minimize thermal effects. A description of the telescope can be found in literature [1], [2]. We describe in the following--in somewhat more detail--only those parts of the telescope which seem to be immediately related to the radio frequency characteristics of the telescope.

(i) Reflector

The reflector consists of 60 individual aluminum panels. These panels are made of 1/8" aluminum, spotwelded to a rigid tube structure. The size of the panels is shown in Fig. 1a. The surface of the panels is painted with a special paint which has low electric losses. This paint is to Rohr Aircraft Corporation Process Specification entitled "Application of Diffuse Reflecting

Coatings for Solid Faced Antenna Reflectors." It consists of:

1. Wet wash primer to Mil-C-8514
2. Zinc chromate primer to Mil-P-8585
3. 3rd - 2 coats Triangle Paint Co.,
Triangle No. 6 paint.

The painting of the reflector was done by Observatory personnel.

The position of each panel can be adjusted by means of three or four jacks, depending on panel location. Four target points were marked on each panel for the optical survey. This survey technique and its results are described in a separate report by C. M. Wade [3].

A structural deflection analysis of the 140-foot reflector due to gravity and wind loading was made by Simpson, Gumpertz and Heger, Inc., under contract to Stone and Webster Engineering Corporation. This report is available in the 140-foot files.

(ii) Feed Support and Sterling Mount

The feed support consists of four feed support legs. These legs are made of aluminum tubes. A structural analysis by W. Horne has shown that the feed support in its original design would have a lateral deflection of 44.5 mm between the positions $z = 0^\circ$ and $z = 90^\circ$. The legs were then reinforced by fins. The analysis for the reinforced structure yielded a total deflection of 19 mm. Figure 1b shows the most important measures of the reflector.

The focus-polarization system of the telescope was constructed by the Sterling-Detroit Company of Detroit, Michigan, to specifications given by the NRAO.

The Observatory specifications were: Axial focus travel of 999 mm with a maximum axial deflection of 0.5 mm; polarization rotation from 0° to 450° with a maximum lateral deflection of 0.025 mm. More detailed specifications are given in [4].

Focus travel is driven through gearing to four lead screws (① in Fig. 2). Alongside each lead screw, which are spaced by 90°, are chrome plated guide tubes and mating ball bushings (②).

Polarization movement is accomplished about a large bearing (③), that is a combination roller thrust, plastic and stainless steel ball bearing. This focus-polarization system is welded through four clips (④) to the "inner doughnut ring" (⑤). The system is designed to take radiometer boxes (⑥) up to a total weight of 1000 lbs., without exceeding the maximum deflections as given in the NRAO specifications.

Two identical Perkin-Elmer brush encoders (specially modified for this purpose) are used to indicate both focus and polarization position. Both units provide 10,000 counts full scale with an accuracy of ± 1 count. The position readout associated with the encoders include necessary register, storage, code translator and lighted display. The stored information is strobed out in parallel 8421 BCD. (⑦) shows drive motor (DC motor) and encoder for the polarization movement; (⑧) shows drive motor and encoder for the axial focus movement.

Fig. 3 shows how the focus and polarization system is attached to the feed support legs (③). The "inner doughnut ring" (①) is connected to the "outer doughnut ring" (②) through four fins (④), which are welded to the inner and outer ring, respectively.

(iii) Servo-mechanism and Resolver Position Readout System

The servo-mechanism is an electro-mechanical system. There are 400 Hz command resolvers attached to the pilot drive and similar comparison resolvers are attached to the input shaft of the gear reducers. The error signals between command and comparison resolvers are used to command the hydraulic motors. This system, which has been built by General Dynamics/Electric Boat, is described in detail in [5].

A second independent resolver system is used for the telescope position indication. The command resolvers--Ferrand 10 kHz inductosyns--are attached directly to the declination and polar shaft, respectively. The comparison resolvers are attached to the readout dials on the control desk.

There are two modes of operating the servo-system of the 140-foot telescope.

a) The "coarse" mode

The 400 Hz resolvers on the gear reducers are used as comparison resolvers.

b) The "fine" mode

400 Hz resolvers are mechanically coupled to the 10 kHz resolvers on the dial outputs. These 400 Hz resolvers are then used as comparison resolvers.

In the case of the "fine" mode, oscillations can occur if the telescope is moved on a fast rate. Therefore, in all programs where quick position changes and short tracks are used successively, the "coarse" mode is used. In programs, however, like line measurements, lunar occultations, etc., where

long trackings are interrupted by only occasional small position corrections, the "fine" mode is used.

The Farrand inductosyns are coupled to polar and declination shaft by means of double-bellow couplings which take care of small axial and radial movements of the shafts.

I. c. Measuring Techniques

To test the telescope one has to measure primarily the focal length, the pointing, the aperture and beam efficiency, and the antenna pattern of the telescope. The corresponding measuring technique is well known if strong point sources are available. At very short wavelengths, however, there is a lack of strong point sources. We will therefore review briefly the measuring technique using extended sources.

(i) Beam shape and half power beam width (HPBW)

If the brightness distribution of the source can be approximated by a gaussian function, the antenna HPBW is

$$(1a) \quad \theta_A = \left[\theta_{ob}^2 - \theta_s^2 \right]^{1/2}$$

with θ_{obs} the HPW of the observed drift curve and θ_s the HPW of the brightness distribution of the source. The only strong source at short wavelengths, which can be safely approximated by a gaussian function is Taurus A.

More often the drift curves of planets are used to determine the HPBW. The brightness distribution of planets can be more closely approximated by a disk distribution (i.e., constant brightness temperature across a disk with

radius R). The relation between HPW of the observed drift curve and antenna HPBW is in this case [6].

$$(1b) \quad \theta_A = \left[\theta_{\text{obs}}^2 - \frac{\ln 2}{2} (2R)^2 \right]^{1/2} \quad \text{with } \frac{\ln 2}{2} = 0.3466$$

valid for $2R < \theta_A$

Using planets it is in the best case possible to determine the shape of the main beam, but certainly not the side lobes. It can be shown, however, [7] that with some reasonable approximations the shape of the main beam and the first side lobes can be obtained by computing the derivative of the drift curve through the sun. The conditions are that the HPBW of the antenna is small as compared to the diameter of the sun, and that the brightness temperature distribution of the sun can be considered as a step function.

We assume now that the antenna pattern as a function of the variables ξ and η (cartesian coordinates in the principal planes of the antenna) can be separated in the way $f(\xi, \eta) = f(\xi) f(\eta)$ (as it is ~~in~~ the case for a gaussian approximation of main beam and first side lobes). The derivative of the drift curve through the sun is then connected with the antenna pattern by the relation

$$(2) \quad \frac{dT_A(\xi')}{d\xi'} = \text{const.} \cdot f(\xi) \quad \xi = R_s - |\xi'| \quad \text{with } R_s$$

the radius of the sun

Here it is assumed that the drift curve lies in the electrical plane of the antenna ($\eta = 0$) and that $\xi' = 0$ coincides with the center of the sun.

In Fig. 4, curve (a), we show as an example a drift curve through the sun, measured during OP V. The long wings in this drift curve are caused by the error pattern of the telescope (see sect. IIa). Compared to the HPW of the error pattern the curvature of the edge of the moon can no longer be neglected; consequently eq. (2) cannot be applied to that part of the drift curve. In order to separate the diffraction pattern and error pattern, we first compute the derivative of the steep parts of the observed drift curve (a) and obtain the two approximations of the main beam and the first side lobe (curves (b)), which allow an approximate determination of the antenna HPBW θ_A . The main beam of the diffraction pattern in the ξ -direction is approximated in the usual way by

$$(3a) \quad f_m(\xi) = \exp \left\{ - \frac{\xi^2}{(0.6 \theta_A)^2} \right\}$$

If the contribution of both side lobes and error pattern are neglected, the observed drift curve through the sun would be given by the convolution of the gaussian main beam with the step function $H(R_s^2 - \xi'^2)$, which yields

$$(3b) \quad f_m(\xi) * H(R_s^2 - \xi'^2) = \frac{1}{2} A_1 \cdot \begin{cases} \left[1 + \Phi \left\{ \frac{R_s + \xi'}{0.6 \theta_A} \right\} \right] & \xi' < 0 \\ \left[1 + \Phi \left\{ \frac{R_s - \xi'}{0.6 \theta_A} \right\} \right] & \xi' > 0 \end{cases}$$

Φ is the error function.

In order to separate the contribution of the main beam to the observed drift curve we multiply eq. (3b) with a factor A_1 which is varied until we get the best fit with the steep parts of curve (a). That area of the drift curve bound by the dashed-dotted lines is consequently due to the convolution between main beam and brightness distribution of the sun. By subtracting this contribution, we obtain curve (c), which is in essence the convolution of the error pattern with the disk of the sun. As is shown in sect. II.a., the error pattern can be approximated by a gaussian function. Hence, the HPW θ_E of the error pattern can be computed from the HPW θ'_E of curve (c) using eq. (1b) and inserting for R the apparent radius of the sun. We designate the maximum of curve (c) by A_2 . The main beam efficiency can be computed from the ratio A_2/A_1 .

The drift curve (a) in Fig. 4 represents a case where the influence of the error pattern is extremely strong. Otherwise the HPBW of the main beam can be determined by varying both A_1 and θ_A in eq. (3b) until a best fit between observed and computed drift curve is achieved.

(ii) Aperture and Beam Efficiency

The aperture efficiency is defined as the ratio of the effective to the geometrical antenna area

$$(4) \quad \eta_A = A/A_g = A / \left(\frac{\pi}{4} D^2 \right)$$

The latter formula holds for a circular aperture with diameter D. The beam efficiency is defined as that part of the total energy received by the

antenna which is contained within the solid angle Ω'_m around the electrical axis of the telescope

$$(5) \quad \eta'_B = \eta_R (1 - \beta'_m) \quad \text{with} \quad \beta'_m = \frac{1}{\Omega} \int_{\text{stray region}} f d\Omega = 1 - \Omega'_m / \Omega$$

β'_m is the stray factor of the measuring beam, η_R the radiation efficiency (for a more detailed discussion of these parameters look at [6]). Ω is the antenna solid angle and f the normalized power pattern.

If, in fact, the stray region is identical with the main beam region (which is the region bounded by the first minimum in the power pattern) $\beta'_m \rightarrow \beta_m$, the main beam stray factor, and $\Omega'_m \rightarrow \Omega_m$, the main beam solid angle. This main beam solid angle is connected with the HPBW of the telescope Θ_E and Θ_H in the principal planes by $\Omega_m = 1.133 \Theta_E \Theta_H$, as long as the main beam can sufficiently well be approximated by a gaussian function. In this case we define the main beam efficiency by

$$(5b) \quad \eta_B = \eta_R (1 - \beta_m) \quad \text{with} \quad \beta_m = 1 - \Omega_m / \Omega = 1 - \frac{1.133 \Theta_E \Theta_H}{\Omega}$$

Note that the radiation efficiency is already contained in the definition of the aperture efficiency (a fact which is sometimes overlooked). Since the effective antenna area is connected with the antenna solid angle by $A = \eta_R \lambda^2 / \Omega$ (λ = wavelength) aperture and main beam efficiency are related by

$$(6) \quad \eta_A = \eta_B \frac{4\lambda^2}{\pi \Omega_m D^2}$$

It has been found that for an edge taper of -16 to -18 dB, which is normally used in the NRAO telescopes,

$$(7) \quad \frac{\theta_A}{\text{min of arc}} = 4.176 \cdot 10^3 \cdot \lambda/D$$

is a good approximation for the HPBW. Computing the main beam solid angle with eq. (7) shows that one should expect a constant proportionality factor $\eta_A = 0.76 \eta_B$ between aperture and main beam efficiency. This has in fact been confirmed at not too high frequencies. If, however, the HPBW of the telescope at a given wavelength changes with time and/or telescope position, aperture and beam efficiency are no longer proportional and may change in quite different ways.

All telescope calibrations mentioned in this report have been performed by using standard calibration sources whose fluxes or black body temperatures are known with a sufficiently high accuracy. We use for the following measurements mainly the spectra of Taurus A and Virgo A as analyzed in [8]. At the highest frequencies planets are used as calibration sources also. In these cases we state the adopted black body temperatures.

As long as the apparent source diameter is smaller than the HPBW of the telescope, we use the relation

$$(8) \quad S_v = \frac{2kT_A}{A} \frac{\Omega_s}{\Omega'_s}$$

Ω_s and Ω'_s are source solid angle and modified source solid angle, respectively, as defined in [8]. For point sources (app. source diameter $\leq 0.1 \cdot$ antenna HPBW), the correction factor is $\Omega_s/\Omega'_s \sim 1$. In all other cases it is > 1 . In order to correct for any polarization of the source, we take the mean value of two measurements with a difference of 90° in polarization angle. T_A is the maximum antenna temperature, corrected for atmospheric extinction.

Gain and aperture efficiency of a telescope are proportional. The relative changes of these quantities with time and/or telescope position are measured by comparing antenna temperatures (which are corrected for atmospheric extinction). However, the proportionality between aperture efficiency and antenna temperature holds only for point sources. That type of measurement should therefore be done only with point sources.

In the case of planets, usually their black body temperature T_{bb} is given. With $\Omega_s = \pi R_p^2$ (R_p = apparent radius of the planet) the source solid angle of the planet, the corresponding flux density is $S_v = \frac{2k}{\lambda^2} T_{bb} \Omega_s$ and eq. (8) can be used to compute A and η_A . Or the relation

$$(9) \quad T_A = \eta_B T_{bb} \frac{\Omega'_s}{\Omega_m} = T_{bb} \Omega'_s \frac{A}{\lambda^2}$$

can be used to compute either η_A or the main beam efficiency η_B if the main

beam solid angle is known. The modified source solid angle for the case of a disk distribution is

$$(10a) \quad \Omega'_s = 1.133 \theta_A^2 \left[1 - \exp \left\{ - \frac{R_p^2}{(0.6 \theta_A)^2} \right\} \right]$$

Hence

$$(10b) \quad T_A = \eta_B T_{bb} \left[1 - \exp \left\{ - \frac{R_p^2}{(0.6 \theta_A)^2} \right\} \right]$$

If the source is extended, one has to integrate the contour map, which is given in antenna temperature corrected for atmospheric extinction.

This integration yields [6], [8]

$$(11) \quad S = \frac{2k}{\lambda^2 \eta'_B} \int_{\text{contour map}} T_A d\Omega$$

and allows us to compute the beam efficiency η'_B of that solid angle Ω'_m , which is approximately given by the size of the convolved source brightness distribution. If the source solid angle is larger than the main beam solid angle, the beam efficiency derived from eq. (11) is usually considerably larger than the main beam efficiency; this is especially the case if the reflector is operated close to its cut-off frequency.

As a first approximation the brightness distribution of sun or moon can be often treated as a disk of constant brightness distribution T_b . The antenna temperature T_A (corrected for atmospheric extinction), which is measured with the electrical axis of the telescope pointing at the center of the disk, is then

$$(12) \quad T_A = \eta'_B T_b = \eta_R \frac{\pi R^2}{\Omega} T_b$$

with R the radius of the disk. This measurement is often used to determine the influence of the error pattern (see sect. II.a).

(iii) Focusing

In the case of an axial defocusing Δf_{ax} the phase error

$$(13) \quad \beta = \frac{2\pi}{\lambda} \Delta f_{ax} (1 - \cos \theta_o)$$

is introduced. θ_o is the aperture angle. The decrease in gain (or aperture efficiency or antenna temperature of a point source) can be computed for the case of a uniform illumination and a $(1 - r^2)$ tapered illumination [7]. One obtains

$$(14a) \quad G/G_o = \left[\frac{\sin \beta/2}{\beta/2} \right]^2 = 1 - \beta^2/12 + \dots \quad \text{for uniform illumination}$$

and

$$(14b) \quad G/G_o = \left[\frac{\sin \beta/2}{\beta/2} \right]^4 + 4/\beta^2 \left[\frac{\sin \beta}{\beta} - 1 \right]^2 \approx 1 - \beta^2/18 + \dots$$

for a $(1 - r^2)$ tapered illumination.

We measure the change in gain by changing the focal length and observing the relative change of the antenna temperature of a point source. These values are then normalized to the maximum antenna temperature $T_{A \text{ max}}$. The curves $T_A(\Delta f_{ax})/T_{A \text{ max}}$ are called the focusing curves; for the taper used in the NRAO telescopes these curves are found to lie between the theoretical curves computed from eqs. (14a and 14b). Curve (a) in Fig. 5a shows such a focusing curve, measured with the 140-foot telescope at 2 cm wavelength (OP VII).

Apart from a decrease in gain, the phase error β introduced by the axial defocusing causes an increase in both the nearby side lobes and the HPBW of the main beam. The latter effect is shown in Fig. 5b. It is, however, surprising to find that the minimum of the HPBW does not occur at that focal length where we observe the optimum antenna gain as we would expect. Curves (b) and (c) in the figure have been measured with the NRAO 85-foot telescope at 6 and 2 cm, respectively, and using the moon. At 6 cm the main beam area of the telescope has a diameter of approximately 20 min of arc. The observed slower decrease in the antenna temperature is in this case mostly due to the increase in the HPBW. At 2 cm the main beam area has a diameter of about 6 min of arc; in this case the decrease in gain is compensated by both an increase in the HPBW and an increase in the nearby side lobe level. This effect is discussed in more detail in [7]. Of importance for the problem of focusing a telescope

is the fact that the line of symmetry of a focusing curve obtained with an extended source and the minimum HPBW do not coincide with the maximum antenna gain as measured with a point source. This effect imposes a serious limitation on using extended sources for focusing.

A radial defocusing introduces a linear and cubic phase error. The linear phase error causes a beam tilt only. The beam tilt angle is B (= beam factor) times smaller than the tilt angle of the phase center of the feed. For the F/D ratio of 0.425, which most of the NRAO telescopes have, this beam factor is calculated to be $B = 0.87$ (Baars, private communication); measurements with the 300-foot telescope yielded a value $B = 0.85$ [11]. Fig. 6 shows the decrease in gain and the increase of the coma side lobe, computed for the F/D ratio 0.425 and the taper preferably used in the NRAO telescopes (Baars, private communication). Obviously the decrease in gain for a given radial defocusing Δf_{ax} is only a small fraction of the gain change due to an axial defocusing by the same amount.

II. RANDOM AND LARGE SCALE REFLECTOR DEVIATIONS

II. a. Short Review of Antenna Tolerance Theory

We use the results of the antenna tolerance theory developed by Ruze [9] [10], with some practical modifications introduced in [6] and [11]. The most important results of Ruze's theory have been experimentally verified in the two latter papers.

The effect of random errors on the telescope characteristics can be completely described if both their rms phase error $\langle \delta^2 \rangle_{rms}$ and their correlation length l are known. The square phase error $\langle \delta^2 \rangle$ is connected with the square reflector deviation $\langle d^2 \rangle$ by

$$(15) \quad \langle \delta^2 \rangle = 16\pi^2 \langle d^2 \rangle / \lambda^2$$

$\langle d^2 \rangle$ is a mean square value weighted for the illumination function. For a non-shallow reflector the deviation Δz measured in the z-direction and Δn measured in the direction normal to the surface are connected with d by

$$(16) \quad d = \frac{\Delta z}{1 + (r/2F)^2} = \frac{\Delta n}{\sqrt{1 + (r/2F)^2}}$$

with r the distance from the axis of the paraboloid. For $F/D = 0.425$ these factors have the numerical values of $\overset{0.75}{\cancel{0.34}}$ and $\overset{0.86}{\cancel{0.49}}$, respectively [10].

Ruze and Scheffler (see [6]) have shown that the power pattern of an aperture with random phase errors can be represented by the superposition of the diffraction pattern f_D with an error pattern f_E whose shape depends on both $\langle \delta^2 \rangle$ and ℓ

$$(17) \quad \overline{f(\theta, \phi)} = f_D(\theta, \phi) + f_E(\theta, \langle \delta^2 \rangle, \ell)$$

In the following, we call a reflector, whose error pattern can be neglected, a "perfect" reflector, as compared to an "imperfect reflector" whose error pattern has to be considered in the computation of the antenna characteristics.

The error pattern is given by the expression

$$(18) \quad f_E(\theta, \overline{\delta^2}, \ell) = \frac{4\ell^2 \overline{\delta^2}}{\eta_{A_0} D^2} \sum_{n=1}^{\infty} \frac{[\overline{\delta^2}]^{n-1}}{n! n} \exp\{-n^2 \ell^2 \theta^2 / n\lambda\}$$

$$\approx \frac{4\ell^2}{\eta_{A_0} D^2} [e^{\overline{\delta^2}} - 1] \cdot \begin{cases} \exp\{-\pi^2 \ell^2 \theta^2 / \lambda^2\} \sqrt{\frac{P_{ov}}{\overline{\delta^2}}} \leq 1 \\ \frac{1}{\overline{\delta^2}} \exp\{-\pi^2 \ell^2 \theta^2 / \lambda^2 \overline{\delta^2}\} \sqrt{\frac{P_{ov}}{\overline{\delta^2}}} \geq 1 \end{cases}$$

with D the diameter of the aperture and η_{A_0} the aperture efficiency of the perfect reflector.

The rigorous expression has been derived by Ruze; the approximation is due to Scheffler. We call the aperture with phase errors imperfect, without phase errors perfect. The antenna solid angle of the imperfect aperture is obtained by integrating eq. (17) and substituting eq. (18). With $\Omega_0 = \int_{4\pi} f_D d\Omega$ the solid angle of the perfect aperture, the integration yields

$$(19) \quad \Omega = \int_{4\pi} \overline{f(\theta, \phi)} d\Omega = \Omega_0 + \Omega_0 (e^{\langle \delta^2 \rangle} - 1) = \Omega_0 e^{\langle \delta^2 \rangle}$$

The antenna gain at a given direction θ, ϕ is obtained by multiplying the pattern of the imperfect reflector, eq. (17) by $4\pi/\Omega$. Substituting eqs. (18) and (19), we obtain with $G_0 = 4\pi/\Omega_0$ the gain of the perfect reflector,

$$(20a) \quad G(\theta, \phi) = G_o e^{-\langle \delta^2 \rangle} + \frac{4\pi^2 \ell^2}{\lambda^2} \left[1 - e^{-\langle \delta^2 \rangle} \right] \begin{cases} \exp \left\{ -\frac{\pi^2 \ell^2 \theta^2}{\lambda^2} \right\} & \text{for } \langle \delta^2 \rangle \leq 1 \\ \frac{1}{\langle \delta^2 \rangle} \exp \left\{ -\frac{\pi^2 \ell^2 \theta^2}{\lambda^2 \langle \delta^2 \rangle} \right\} & \text{for } \langle \delta^2 \rangle \geq 1 \end{cases}$$

and consequently for the axial gain ($\theta = 0$)

$$(20b) \quad G = G_o e^{-\langle \delta^2 \rangle} + \frac{\eta_R 4\pi^2 \ell^2}{\lambda^2} \left[1 - e^{-\langle \delta^2 \rangle} \right] \cdot \begin{cases} 1 & \text{for } \langle \delta^2 \rangle \leq 1 \\ \frac{1}{\langle \delta^2 \rangle} & \text{for } \langle \delta^2 \rangle \geq 1 \end{cases}$$

or

$$(20c) \quad G/G_o = e^{-\langle \delta^2 \rangle} + \frac{\eta_R}{\eta_{A_o}} \left(\frac{2\ell}{D} \right)^2 \left[1 - e^{-\langle \delta^2 \rangle} \right] \begin{cases} 1 & \text{for } \langle \delta^2 \rangle \leq 1 \\ \frac{1}{\langle \delta^2 \rangle} & \text{for } \langle \delta^2 \rangle \geq 1 \end{cases}$$

A similar relation holds for the ratio η_A/η_{A_o} of the aperture efficiency of the imperfect reflector. Only if the contribution of the error pattern can be neglected the decrease in gain due to the phase error $\langle \delta^2 \rangle$ is described by $\exp \{-\langle \delta^2 \rangle\}$. Since ℓ/D values of 10^{-1} or smaller are typical, the ~~first~~ approximation of eq. (20c) by the first term on the right side is correct in most cases. This relation has been experimentally checked in [6] and [11]. The maximum gain of the imperfect reflector occurs at the wavelength $\lambda = 4\pi \langle d^2 \rangle_{\text{rms}}$, where a tolerance loss of 4.3 dB is incurred.

A different situation is found, however, if one considers the beam efficiency rather than the aperture efficiency. In this case the radiation received in the error pattern can not be neglected. Although the total

energy contained in the error pattern depends only on the mean square phase error, both HPBW and peak value of the error pattern depend strongly on the correlation length.

For the HPW of the error pattern one obtains

$$(24a) \quad \frac{\theta_E}{\text{min of arc}} = \begin{cases} 1.822 \cdot 10^3 \lambda/\ell & \text{for } \langle \delta^2 \rangle \leq 1 \\ 2.290 \cdot 10^4 \cdot \langle d^2 \rangle_{\text{rms}}/\ell & \text{for } \langle \delta^2 \rangle \geq 1 \end{cases}$$

or expressed in main beam HPBW's, substituting eq. (7)

$$(24b) \quad \frac{\theta_E}{\theta_A} = \begin{cases} 0.436 D/\ell & \text{for } \langle \delta^2 \rangle \leq 1 \\ 5.484 D \langle d^2 \rangle_{\text{rms}}/\lambda \ell & \text{for } \langle \delta^2 \rangle \geq 1 \end{cases}$$

Since $D/\ell > 10$ in most cases of practical interest, one can use the peak value of the error pattern in order to estimate the increase in the side lobe level due to the error pattern.

$$(25) \quad \text{Level of first side lobe} = \frac{1}{\eta_{A_0}} \left(\frac{2\ell}{D} \right)^2 [e^{\langle \delta^2 \rangle} - 1] \begin{cases} 1 & \text{for } \langle \delta^2 \rangle \leq 1 \\ \frac{1}{\langle \delta^2 \rangle} & \text{for } \langle \delta^2 \rangle \geq 1 \end{cases}$$

In order to obtain a general expression for the beam efficiency, we have to evaluate the integral

$$\eta_B' = \frac{\eta_R}{\Omega_0 e^{\langle \delta^2 \rangle}} \int \{f_D(\theta, \phi) + f_E(\theta, \langle \delta^2 \rangle, \ell)\} d\Omega$$

measuring
beam region

For the integral over the diffraction pattern, we substitute $\Omega'_m = \Omega_m + (\Omega'_m - \Omega_m)$, with Ω_m the main beam solid angle and

$$\eta_{R \Omega'_m / \Omega_m} = \eta_{B_o} \quad \text{the main beam efficiency of the perfect reflector}$$

$$\eta_{R \Omega'_m / \Omega_o} = \eta'_{B_o} \quad \text{the measuring beam efficiency of the perfect reflector}$$

The integration over the error pattern can be performed for a circular measuring beam region with angular radius R. Substituting for the error pattern f_E eq. (18), we obtain

$$(26) \quad \eta'_B = e^{-\langle \delta^2 \rangle} \left[\eta_{B_o} + (\eta'_{B_o} - \eta_{B_o}) \right] + \eta_R \left[1 - e^{-\langle \delta^2 \rangle} \right] \cdot$$

$$\cdot \begin{cases} \left[1 - e^{-\frac{\pi^2 \ell^2 R^2}{\lambda^2}} \right] & \text{for } \langle \delta^2 \rangle \leq 1 \\ \left[1 - e^{-\frac{\pi^2 \ell^2 R^2}{\lambda^2 \langle \delta^2 \rangle}} \right] & \text{for } \langle \delta^2 \rangle \geq 1 \end{cases}$$

For $R \rightarrow \infty$; $\eta'_{B_o} \rightarrow \eta_R$ and consequently $\eta'_B \rightarrow \eta_R$ as we would expect.

If we integrate over that part of the pattern where the error pattern deviates significantly from zero, we obtain

$$(27) \quad \frac{\eta'_B}{\eta'_{B_o}} = e^{-\langle \delta^2 \rangle} + \frac{\eta_R}{\eta'_{B_o}} \left[1 - e^{-\langle \delta^2 \rangle} \right]$$

This equation bears some resemblance to eq. (20c) for the decrease in axial gain. The decrease of both gain and beam efficiency of the diffraction pattern is compensated somewhat by the increase in gain and beam efficiency of the error pattern. However, this compensation is, in the case of the beam efficiency, about a factor of $(D/2\ell)^2$ stronger. This explains the different behavior of aperture efficiency and beam efficiency, if a change in telescope position is connected with a change in the mean square phase error introduced by the reflector.

The integration over the contour map of an extended radio source conforming to eq. (11) will, in most cases, be extended over the source solid angle rather than over the whole error pattern. In order to estimate the influence of the error pattern one has to estimate the radius R of the solid source angle and insert it in eq. (26). For not too large values of R (compared with the HPW of the error pattern) we can use a first order approximation of the exponential functions in eq. (26). Expressing then the radius R in units of the HPBW of the diffraction pattern, one obtains

$$(28) \quad \eta'_B = e^{-\langle \delta^2 \rangle} \left[\eta_{B_0} + (\eta'_{B_0} - \eta_{B_0}) \right] + \eta_R \left[1 - e^{-\langle \delta^2 \rangle} \right] \cdot \left(\frac{\ell}{D} \right)^2 \cdot \left(\frac{R}{\theta_A} \right)^2 \cdot 14. \begin{cases} 1 & \text{for } \langle \delta^2 \rangle \leq 1 \\ \frac{1}{\langle \delta^2 \rangle} & \text{for } \langle \delta^2 \rangle \geq 1 \end{cases}$$

If the integration is made over the main beam area, i.e., the solid angle within the first minimum of the diffraction pattern, $R/\theta_A \approx 1/2$.

Comparison with eq. (20c) shows that the compensation of the decrease in the main beam efficiency of the diffraction pattern due to the increase of the beam efficiency of the error pattern is stronger by a factor $1 + \frac{R}{\theta_A}$ as compared to the compensation of the aperture efficiency by the same effect.

As a numerical example, we consider the 140-foot telescope at $\lambda = 2$ cm. For $\langle d_{rms}^2 \rangle = 0.9$ mm, we obtain $\langle \delta^2 \rangle = 0.32$. For $\langle d_{rms}^2 \rangle = 2$ mm, we obtain $\langle \delta^2 \rangle = 1.52$. This is the range in which the phase error changes with telescope position. With $R/\theta_A = 2$ and $D/\lambda = 30$, we find that the error pattern contributes ~~2.5%~~^{0.3%} to the beam efficiency in the first case and ~~16%~~^{2%} in the second case.

II. b. Measurement of Aperture and Beam Efficiency at Various Wavelengths. Determination of the RMS Reflector Deviation and the Aperture Efficiency of the Perfect Reflector

Using the techniques described in sect. I.c., HPBW, aperture and beam efficiency of the 140-foot telescope have been measured at various wavelengths. The results are compiled in Table 2.

Table 2

λ/cm	OP	HPBW min arc	η_A %	η_B %	Calibration Source	Observers
11.1	II	11.8	59	78	Hydra A; $S_{2.7} = 21.8$ f.u.	Kellermann & Pauliny-Toth
5.99	I	6.3 ; 6.45	53	81	Integr. of Tau A; Cyg A; Vir A. Flux densities from [8]	Henderson & Mezger
5.99	IV	5.4 ; 6.3	63	83	Hydra A; $S_6 = 13.0$ f.u.	Kellermann & Pauliny-Toth
1.95	III	1.9	43	54	Integr. of Tau A; Cyg A; Vir A. Flux densities from [8]	Baars & Mezger
1.95	VII	2.0 ; 2.0	37	49	" " "	Schraml & Mezger
0.95	V	1.35; 1.02	15	23	Jupiter $T_{pb} = 140^\circ K$	Baars

Since we expect the relation $\eta_A(\lambda) = \eta_{A_0} e^{-16\pi^2 \frac{\langle d^2 \rangle}{\lambda^2}}$, we plot $\log \eta_A(\lambda)$ against $1/\lambda^2$, and fit a straight line through the measured points. The slope of this line of best fit yields $\langle d^2 \rangle$, the intersection of the line with the axis $1/\lambda^2 = 0$ yields the aperture efficiency of the perfect reflector. We obtained

$$\langle d^2 \rangle_{\text{rms}} = 0.92 \text{ mm}$$

$$\eta_{A_0} = 0.60$$

II. c. Variation of Aperture and Beam Efficiency with Telescope Position

Aperture and beam efficiency are connected by eq. (6). In the case of a perfect reflector the proportionality factor between the two quantities should be a constant. In the case of an imperfect reflector the proportionality factor may change with both telescope position and time or meteorological conditions. In this section we are concerned with the variation of aperture and beam efficiency with telescope position. The measuring technique used for this investigation is described in sect. II.c. (ii). In the case of a polar mounted telescope the variation of both characteristics as a function of hour angle can be measured with one source. In order to investigate the declination dependence a set of different radio sources have to be used. The accuracy of the latter measurement is severely limited by the restricted knowledge of relative flux densities of radio sources in the short cm wavelength range.

Figure 7 shows the "gain" variation measured during OP I and II. But since the sources used for these measurements are not point sources, the actual decrease in aperture efficiency may be stronger. Baars and Mezger [12] deduced from this gain variation an increase in the random reflector deviations from 0.92 mm at the meridian to 1.44 mm at large hour angles.

Kellermann and Pauliny-Toth obtained curves for the variation of aperture efficiency (and gain) by measuring the peak antenna temperature produced by point sources over a large range of hour angles and declinations. Their results are summarized in curves a, b, and c of Fig. 8; we have only reduced their original measurements by correcting for atmospheric extinction, using a zenith extinction of $p = 0.992$ (at $\lambda = 6$ cm) and $p = 0.975$ (at $\lambda = 1.95$ cm). The similarity of curves b and c show that in a first order approximation the decrease in aperture efficiency depends mainly on the zenith distance.

Mezger and Schraml measured the variation of the beam efficiency by integrating galactic HII-regions with small apparent diameter, like K 45, K 47, AMWW 40, Orion A and IC 434. Once the flux of these HII regions has been measured accurately at $\lambda = 6$ cm their thermal spectra can be safely extrapolated by assuming a $\nu^{-0.1}$ dependence of the flux density.

Curve d in Fig. 8 shows the relative change of beam efficiency at $\lambda = 1.95$ cm (OP VII) as a function of zenith distance. Within the accuracy of the measurements the beam efficiency seems to remain constant at least within the range $z \leq 54^\circ$.

II. d. Variation of Focal Length with Telescope Position

Any deviation of the phase center from the true focal point of the parabolic reflector results in a decrease in gain (sect. II.e). In the measure-

ments described in sec. II.c, we have tried to eliminate this effect by adjusting the focal length for optimum gain before each set of observations. Figs. 9a and 9b show the variation of both focal length and aperture efficiency obtained from observations with three point sources during OP VII. One clearly recognizes an asymmetry in both sets of curves with respect to the meridian. This asymmetry becomes more obvious with decreasing declination.

Fig. 10 summarizes the change of focal length observed during OP I ($\lambda = 6$ cm) and OP VII ($\lambda = 2$ cm). Since this effect should not depend on wavelength both sets of observations can be combined. The change of focal length with hour angle shows again an asymmetry. The change of focal length with declination shows a general decline and a dip at the declination 10° . This declination coincides roughly with the declination $\delta = 12^\circ$ at which the southern feed support legs come into a vertical position, and hence may become unstable.

The general tendency found in the curves in Figs. 9 and 10 shows a decrease in the indicated focal length of the 140-foot telescope with increasing zenith distance. Wade's measurements [3] have shown that this variation of focal length obtained from radio observations can only partly be explained by a sag in the feed support legs. There seems to exist a large scale deflection of the 140-foot reflector, which renders the paraboloid deeper at extreme telescope positions. More evidence for such an effect is given in sect. II.h.

II. e. Variation of Aperture and Beam Efficiency and Antenna HPBW with Axial Focus Position

The results of our investigations of the effect of axial defocusing on aperture and beam efficiency and HPBW are given in Figs 5a and b. Although curves a, b, and c in Fig. 5a have been obtained with the 85-foot telescope,

they can be applied to the 140-foot telescope too. Curve (a) shows the variation of aperture efficiency since measured with a point source. The optimum value of this curve indicates the position of the focal point. Curves b and c show the variation of the beam efficiency with axial focus position for two different source sizes. This effect has been discussed in more detail in sect. I.c.(ii). The axes of symmetry of the beam efficiency curves are shifted towards the reflector with respect to the true focal point. Fig. 5b shows the variation of HPBW, measured with the 140-foot telescope during OP VII. This variation has been measured in one principal plane of the telescope only. It shows, however, that the minimum HPBW in this plane occurs at a focus position shifted away from the reflector with respect to the true focal point.

An axial defocusing should introduce phase errors of even order only. Hence one would expect a change of telescope characteristics symmetrical with respect to the true focal point. Why the observed variations of beam efficiency and HPBW show a deviation from this predicted symmetry is not yet understood.

II. f. Misalignment of the Rotation Axis of the
Sterling Mount with Respect to the
Electrical Axis of the 140-foot Reflector

Such a deviation should introduce a decrease in gain which would become stronger as the wavelength of observation becomes shorter. It also would introduce an asymmetry in the side lobes (coma lobe). It is therefore of importance to check the alignment between rotation axis of the Sterling mount and the electrical axis.

The electrical axis of the telescope is defined as the axis where maximum antenna gain is observed when the phase center of the feed is moved in radial direction.

The original adjustment of the feed support position is based on the assumption that the electrical axis of the 140-foot reflector coincides with the mechanical axis of the paraboloid of best fit of the adjusted panels. A reticule was fixed in the center of the inner doughnut ring (Fig. 3). The telescope was pointed toward zenith and a theodolite was adjusted in the center of the vertex of the reflector. With the theodolite pointed towards zenith the feed support was adjusted in such a way that i) the center of the reticule coincided with the mechanical axis of the reflector, and ii) this coincidence was maintained when the focal length was changed. Since this latter condition requires an axial movement of the focusing mount, its accomplishment means that the axial travel of the mount occurs parallel to the mechanical axis of the reflector.

The radio test of this alignment was done in the following way. During OP I the feed horn was laterally displaced by 3 HPBW's (feed tilt, not beam tilt; this means $B = 1$ and $1 \text{ HPBW} = 32 \text{ mm}$)*. Then the Sterling mount was rotated in steps of 30° , the source was peaked up and its maximum antenna

*In a later set of similar observations we used the sky horn, which is displaced from the center feed but looks towards the reflector. A source in the center feed produces in a beam switched radiometer a positive signal, in the feed horn it produces a negative signal. The observations in the offset feed were normalized with respect to the signal measured in the center feed. This procedure eliminates automatically any effect of gain variation of the telescope or polarization of the radio source.

temperature was recorded. Fig. 11a shows the result of measurements for two radio sources. If rotation axis and electrical axis coincide we would expect a straight line. If there is a deviation between the two axes, one expects a sinusoidal variation of the antenna temperature measured in the offset feed. We determine from this curve i) the position angle of the feed $\phi_f(\text{max})$ at which the maximum antenna temperature is observed and the ratio $T_A(\text{min})/T_A(\text{max})$. Fig. 11b shows the geometry of feed, rotation axis and electrical axis involved in this discussion. Position angle of beam and feed are displaced by 180° . The feed travels on a concentric circle around the rotation axis of the Sterling mount. It can easily be shown that the maximum antenna temperature is found at that position angle where the beam, electrical and rotation axes lie on one straight line and the beam and electrical axes lie on the same side of the rotation axis. In order to get coincidence between rotation axis and electrical axis, the feed support has to be moved in the direction $\phi_f(\text{max}) + 180^\circ$.

The amount of the displacement $\Delta\theta = \Delta(\text{electr. axis-rotation axis})$ can be determined from the ratio $T_A(\text{min})/T_A(\text{max})$ of the observed curve Fig. 11a. Fig. 11c shows the variation of aperture efficiency (and hence of the antenna temperature of a point source) as a function of feed tilt as computed by J.W.M. Baars. The variation $T_A(\text{min})/T_A(\text{max})$ is then computed in the following way. We assume a given angular displacement $\Delta\theta$ between electrical and rotation axis, e.g., 1 HPBW. The maximum antenna temperature is found from the curve T_A in Fig. 11c at the position 3 HPBW - 1 HPBW (since the offset feed is displaced by 3 HPBW's); the minimum antenna temperature is obtained from the value of the same curve at the position 3 HPBW + 1 HPBW. In a similar way the ratio

$T_A(\text{min})/T_A(\text{max})$ can be computed for any given angular displacement $\Delta\theta$, yielding the curve $T_A(\text{min})/T_A(\text{max})$ in Fig. 11c.

The observed curve, Fig. 11a, cannot be approximated by a sine wave (indicated by the dashed curve); we do not understand why. If we assume that the dashed curve represents the true variation of antenna temperature, we obtain the values $\phi_f(\text{max}) = 215^\circ$; $T_A(\text{min})/T_A(\text{max}) = 0.9$. Substituting the latter value in the diagram, Fig. 11c, we obtain for the angular displacement between electrical and rotation axis $\Delta\theta \cong 0.8 \text{ HPBW (feed tilt)} = 5 \text{ min arc}$. The true displacement is found from

$$\Delta(\text{axis}) = \frac{\Delta\theta}{\text{min arc}} 2.91 \cdot 10^{-4} \cdot F = 26.5 \text{ mm}$$

where $F = 18.2 \text{ m}$ the focal length of the 140-foot telescope. In order to correct this deviation the feed support has to be moved in the direction $\phi_p = 215^\circ + 180^\circ = 35^\circ$ by 26.5 mm. The loss in gain and aperture efficiency introduced by this lateral displacement is at $\lambda = 6 \text{ cm}$ only 0.75%. At $\lambda = 9.5 \text{ mm}$ however the corresponding loss in gain runs up to about 22%.

Many more measurements of this type have to be made at various telescope positions to determine the deviations between electrical and rotation axis before any adjustment should be made. The technique described in this section is, however, new. A detailed description seems therefore to be justified.

II.g. Determination of Error Pattern and Correlation Length

It was shown in sect. II.a. that the size of the error pattern depends on both the RMS reflector deviation (and rms phase error) and the correlation

length of these deviations. Reflector deviations and correlation length depend usually on the telescope position. If, in addition, large scale deflections are superimposed on the random reflector deviations, we can no longer expect that the relations derived in sect. II.a. will yield meaningful results if applied to the observed telescope characteristics.

The error pattern can be directly measured only at those frequencies where the phase error introduced by the reflector deviations is close to or larger than unity. Investigations of the error pattern of the 140-foot telescope have therefore been limited to the wavelengths 1.95 cm and 0.95 cm. It has been explained in sect. I.c.(i) how the shape of the error pattern can be determined from drift curves through the sun or the moon. In this way the following HPW's of the error pattern have been measured.

Table 3

λ/cm	$\theta_E/\text{min arc}$	z	Source	$\langle d^2 \rangle_{\text{rms}} \text{ adopt.}$	$\langle \delta^2 \rangle$	l/cm
0.95	21.5	24°	moon	0.92 mm	1.49	98
0.95	31.0 \pm 0.5	60°	sun	1.44 mm	3.63	153
1.95	62.0 \pm 2.0	34°	sun	1.00	0.415	57

The third column of this table gives the zenith distances at which the measurements have been performed, using the sources indicated in the fourth column. The fifth column gives the rms reflector deviation which has been adopted to compute the correlation lengths using eq. 24a. For $\langle \delta^2 \rangle \leq 1$, we would expect a decrease of the HPW of the error pattern proportional to the wavelength. For phase errors $\langle \delta^2 \rangle \geq 1$, the HPW should become wavelength

independent. Both the observed HPW's Θ_E and the different values of the correlation lengths (last column) derived from these observed values show that one has to be cautious in applying antenna tolerance theory of random reflector deviations to the 140-foot telescope.

In order to investigate this effect in more detail we measured the measuring beam efficiency at $\lambda = 0.95$ cm at three declinations using the sun and the moon (adopted brightness temperatures: $\langle T_{bb} \text{ (moon)} \rangle = 180^\circ\text{K}$; $T_{bb} \text{ (sun)} = 8 \times 10^3^\circ\text{K}$). The following results were obtained:

$$\eta_B' = 0.64 \quad (\delta = +23^\circ, \text{ moon}); \quad \eta_B' = 0.445 \quad (\delta = -7^\circ, \text{ moon});$$

$$\eta_B' = 0.385 \quad (\delta = -23^\circ, \text{ sun})$$

These values are plotted in Fig. 12a as a function of declination. The three points can be connected by a smooth curve.

In sect. II.a. we have derived an expression for the beam efficiency of an imperfect reflector. We rewrite eq. (26) in the form

$$(29) \quad \eta_B' = e^{-\langle \delta^2 \rangle} [\eta_{B_o}' + (\eta_{B_o}' - \eta_{B_o})] + [1 - e^{-\langle \delta^2 \rangle}] \cdot \eta_R$$

$$\cdot [1 - \exp \{-R^2 / (0.6\Theta_E)^2\}]$$

$$\text{with } \Theta_E = 2\sqrt{\ln 2} \frac{\lambda}{\pi l} \begin{cases} 1 & \text{for } \langle \delta^2 \rangle \leq 1 \\ \frac{1}{\langle \delta^2 \rangle} & \text{for } \langle \delta^2 \rangle \geq 1 \end{cases}$$

the HPW of the error pattern. This relation has been evaluated for the range of phase errors $1.2 \leq \langle \delta^2 \rangle_{\text{rms}} \leq 1.9$; this corresponds at the wavelength

$\lambda = 0.95$ cm to a range of rms reflector deviations of $0.91 \text{ mm} \leq \langle d^2 \rangle_{\text{rms}} \leq 1.44 \text{ mm}$. We have assumed a beam efficiency of the diffraction pattern over the solid angle subtended by the sun or moon $\eta_{B_0} + (\eta'_B - \eta_{B_0}^{\text{err}}) = 0.79$. Hence the only variables in eq. (29) are the phase error and the HPW of the error pattern. Fig. 12b shows the result of this evaluation as a family of curves with the HPW of the error pattern as parameter. For a narrow error pattern the beam efficiency is nearly independent of the phase error, since the radiation energy lost in the main beam is completely compensated by the increase in radiation energy received by the error pattern. Only at relatively large values of θ_E do we compute a noticeable decrease of the beam efficiency with increasing phase error.

This diagram shows clearly that it is not possible to explain the observed change in beam efficiency with declination by an increase of the reflector deviation alone. From measurements of the change of aperture efficiency with declination (sect. II.c.) we have concluded that the rms reflector deviation is $\langle d^2 \rangle_{\text{rms}} = 0.92$ mm close to the zenith and about 1.44 mm at large zenith distances. We substitute the maximum and minimum measured beam efficiency at the corresponding reflector deviations in the diagram 12b and connect the two points by a straight line (or any other reasonable curve). We see then that the observed decrease in beam efficiency can be explained only if we assume that the HPW of the error pattern increases from 28' close to the zenith to about 40' at low declinations. Table 3 shows that the observed HPW's of the error pattern increases indeed by about 10'. The measured HPW's are, however, too small by about 8'. In this computation it has been assumed that the main beam efficiency of the diffraction pattern remains constant. It has been found, however, that for large phase errors the main beam becomes distorted. This would, of course, affect the main beam efficiency too.

The observations and their interpretation indicate strongly an effect of large scale reflector deviations of the 140-foot reflector at least at larger zenith distances. More evidence for large scale reflector deviations is given in the following sect. II.h.

II.h. Variation of Beam Shape with Telescope Position;
Large Scale Reflector Deviations

During the initial telescope calibration at the beginning of OP VII, it was found that at low declinations and/or large hour angles the main beam of the diffraction pattern became distorted. A similar effect had already been found during OP V; but since the beam shape measurements were then made with the sun, we were not too sure about the results.

As a typical example, Fig. 13a shows cross sections through the main beam of the 140-foot telescope, measured at $\lambda = 1.95$ cm (OP VII) and using Venus ($\delta = -13^\circ$) as test source. The cross sections were measured in α and δ ; at the beginning of each measurement the source was peaked up and the focal length was adjusted for optimum gain. The α -cross sections show at larger hour angles "shoulders", which increase with increasing hour angle. It is interesting to note that the shoulder appears at large h.a. "east" at the west side of the main lobe and vice versa.

The corresponding δ -cross sections show a similar shoulder north of the main beam. The amplitude of this " δ -shoulder" seems less than that of the " α -shoulder" at larger h.a.; on the other hand / does not disappear even at the meridian. α - and δ -shoulders seem to form one secondary maximum. This can be seen from Fig. 13b, where a contour map of 3C 273 has been plotted--one at h.a. $4^h 15^m$ east. At the large hour angle the secondary maximum can be

at the meridian, the other
↑

seen quite clearly; at the meridian a "clean" main beam is observed. It seems that the secondary maximum always appears in a direction opposite to the vector of the gravity force.

The most straight-forward way of interpreting the observed beam distortion would be an analysis of the phase error (and the corresponding reflector deviation) which could cause the observed beam distortion. Such an analysis has not been made. We found, however, some indication concerning the nature of the large scale reflector deviation at large zenith distances from other measurements:

- i) We found that the indicated focal length of the 140-foot telescope gets shorter with increasing zenith distance, (sect. II.d.). Evidently the reflector "folds" inwards, resulting in a shorter focal length.
- ii) During OP V we tried to determine the focal length of the telescope at low declinations ($\delta = -23^\circ$) by changing the focal length and determining the HPBW of the main beam from drift curves through the edge of the sun. We found a focal length of <210 mm in the NS-(δ)-direction and a focal length of 225 mm in the EW-(α)-direction. Although these results have to be considered with caution in the light of the experimental results mentioned in sect. II.e., there seems to be strong evidence that at low declinations the focal point has degenerated into a "focal line".

Based on these observational facts, we adopted as a working hypothesis that the 140-foot reflector folds inward at large zenith distances, but that

these large scale deflections do not result in another paraboloid with only a shorter focal length (homologous deformation) but rather result in an ellipsoid. Such a deformation would yield different focal lengths for different sections of the reflector. In order to support this hypothesis two different sets of measurements were made.

1. The focal length was changed and the beam shape (α - and δ -cross sections) was investigated as a function of focal length. With an elliptical deformation of the reflector one would expect there to be two different focal lengths at which either the α -cross sections or the δ -cross sections through the main beam yield a "clean" beam (i.e., a symmetrical beam with minimum side lobes). Fig. 14 shows the result of such a set of observations made with Venus. The two focal lengths which yield clean beams lie at $f = 200$ mm (δ -cross sections) and 225 mm (α -cross sections). The focal length which yields optimum gain lies at $f = 218$ mm.
2. In the case of a "focal line", we expect a broader focusing curve than in the case of a focal point. Figs. 15a and 15b show focusing curves measured with Virgo A and Venus at various hour angles. The points represent the measurements. The solid curve in each graph represents the focusing curve obtained with 3C 84 at the meridian (where the reflector approximates a paraboloid pretty well). One recognizes that the focusing curves get broader with increasing h.a.

All these measurements are not yet conclusive, but represent a strong evidence for a large scale reflector deviation at large zenith distances. An optical

survey of the reflector at various telescope positions would certainly be the most direct method to determine the reflector shape and deformation.

III. POINTING ERRORS

III.a. Comparison of Pointing Corrections at Various Wavelengths

Figs. 16a and 16b show the declination corrections near 0^h hour angle at 11 cm (September 1965) and at 2 cm (February 1966), respectively.

For the 11 cm curve, the data was obtained over a period of four days and the individual measurements are shown. The scatter is about $1'$ of arc, peak-to-peak. The smooth curve is a least squares fit to an expression involving a refraction term, a bending term and a constant.

The 2 cm curve was obtained over a period of about 24 hours. The individual data points are not shown, but the accuracy is estimated to be $\sim 10''$ of arc. The extent of the curve in declination is severely limited by the lack of small diameter sources strong enough for the pointing program to be carried out in such a short period.

The main difference between the curves is the dip, at declination $+15^\circ$, in the 2 cm curve, which is barely, if at all, visible in the 11 cm curve. This declination corresponds roughly to the point at which the plane of the south-east and south-west feed support legs is vertical. The corresponding curve at 6 cm is intermediate in shape between the curves shown.

The R.A. correction curves are similar at the three wavelengths, but at 2 cm they show some irregularity, again in the range of 0° to 20° declination.

III. b. Remaining Pointing Error after
Correction for Atmospheric Refraction

This is shown in Fig. 16a by the broken curve. The refraction term was obtained from the least squares fit, and its value is about that to be expected at the altitude of Green Bank. The remaining correction varies from its zenith value by $-1.5'$ of arc at declination -40° to $+1'$ of arc at declination $+80^\circ$.

At the declination of $+40^\circ$, the remaining R.A. correction after subtracting refraction increases by about 2^s of H.A. between the meridian and hour angles of $\pm 5^h$. This is somewhat smaller than the value expected on the basis of the bending in declination near the meridian. The reason for this may be that the bending of the feed support structure is not a function of zenith angle alone, but also of the orientation of the feed legs with respect to the horizontal plane.

III. c. Short Term Pointing Errors

By "short term", we mean over periods of a few minutes to a few hours. The pointing observations at 2 cm indicate that such errors are $\sim \pm 10''$, in spite of the fact that the feed assembly was rotated during these measurements. Without feed rotation a repeatability of source position measurements of about 3 sec arc was obtained (OP VII). Measurements at the edge of the sun (OP V) showed a repeatability of 5 sec arc under good observing conditions and 20 sec arc with wind gusts up to 20 mph.

III. d. Daily Pointing Errors

Fig. 17 shows the daily corrections in declination and R.A. for the period February-March 1966 at 2 cm. 3C 84 and 3C 273 were used to obtain these

curves. The transit of 3C 84 occurred in the daytime, that of 3C 273 occurred at night. The peak-to-peak scatter is about $\pm 20''$ in both R.A. and declination. The scatter does not seem to be entirely random: the corrections on consecutive days are correlated. There is no difference between the daytime and nighttime observations. Since 3C 84 is near the zenith, the scatter is not due to day-to-day changes in the atmospheric refraction.

The scatter in the data at 11 cm (Fig. 16a) suggests that such variations in pointing also occur at that wavelength.

III. e. Correlation Between Pointing Errors and Rotation of the Sterling Mount

As mentioned in c, the pointing calibration was carried out with the feed in different position angles, normally in two position angles differing by 90° . From these observations, there is no evidence of any random error introduced by rotation of the feed.

However, during OP VII a direct attempt was made to determine the position accuracy of the 140-foot telescope if the Sterling mount was rotated. The position of 3C 84 at $\lambda = 2$ cm was determined as a function of polarization angle. Measurements were made in steps of 30° . The accuracy of one single reading was determined to be better than 10 sec arc. Fig. 18 shows the result of this set of observations. Each point corresponds to the source position measured at that polarization angle which is indicated in the graph. There is obviously an erratic change in the indicated source position which is by far greater than the inaccuracy of a single reading. The set of measurements corresponds to two full rotations of the Sterling mount from 20° to 380° ,

then back to 20° and again to 380° . It is of interest to note the deviations of the 20° and 380° positions, which should yield the same indicated source positions (apart from a slight correction which is due to the change of the pointing with telescope position). This erratic change of the indicated source position with polarization angle cannot be explained by a deviation between phase center of the feed and rotation axis of the Sterling mount. In this case we would expect to find the indicated source positions lying on a circle.

An indication of what may cause this pointing error of the telescope with rotating the Sterling mount may be obtained from the fact that it was found recently that the front end boxes seem to bend under their own weight. Since the feed is bolted to the front end box, this bending will cause a lateral movement of the phase center and hence a beam tilt.

IV. TIME VARYING EFFECTS

IV. a. Time Variation of Pointing

The pointing curves obtained at 11 cm in September 1965, at 6 cm in January 1966, and at 2 cm in February 1966 are similar in shape. The differences between them can be accounted for by small changes ($\sim 30''$) in the collimation error, that is, by small displacements of the phase centers of the feeds from the axis of the dish.

IV. b. Time Variation of Focal Length

During the 2 cm measurements (OP VII) daily routine checks of the focal length were made. A large scatter was found in the data, but an obvious correlation was found only when the indicated focal lengths were plotted as a function of ambient temperature (Fig. 19). With all parts of the telescope--reflector

and feed support legs--in thermal equilibrium, one would not expect such a temperature dependence since all parts are made of the same material (aluminum). The temperature dependence of the focal length is obviously much stronger during day time. This is a strong indication that we deal with a differential temperature effect which may be due to the fact that reflector and feed support legs have different thermal time constants.

Fig. 20 shows measurements of the focal length using sources at various declinations. In the same graph the ambient temperature is plotted for the time the measurements were made. There is an indication that the asymmetry found in the focusing curves is correlated with the ambient temperature.

IV. c. Time Variation of Aperture Efficiency

During OP VII the relative flux densities of various extragalactic radio sources were observed [13]. The small scatter in the flux density of Virgo A indicates that the aperture efficiency of the 140-foot telescope remains rather constant as long as the telescope is focused for optimum gain. If the decrease in aperture efficiency at $\lambda = 1.95$ cm from 43% (OP III) to 37% (OP VII) is a real effect or rather due to different feeds and errors in the antenna temperature calibration cannot yet be decided.

V. INFLUENCE OF THE ATMOSPHERE

The inhomogeneous structure of the atmosphere will affect the measured characteristics of a radio telescope. This in turn may lead to a misinterpretation of the results of the radio tests of the 140-foot telescope. We therefore decided to investigate a possible influence of the atmosphere.

In subsection a., we start with a short, qualitative introduction to the theoretical work which has been done to date in microwave scintillation.

In subsections b. and c. we describe general methods as well as our adopted observing technique to detect atmospheric effects.

The general theory which describes the influence of an inhomogeneous atmosphere on the characteristics of a single-dish antenna seems to be well established. To apply these theories to cases of practical interest, one has to know some physical parameters of the atmosphere, e.g., correlation length and rms fluctuation of the refractive index. Unfortunately, these characteristics have to date not been investigated with a sufficiently high precision. This may be the reason that the effect of the atmosphere on the characteristics of very large antennas has been apparently grossly overestimated in most theoretical papers.

V. a. Short Review of Microwave Scintillation Theory

Electromagnetic radiation propagating through an inhomogeneous atmosphere suffers from random phase and amplitude fluctuations. It is generally accepted that in the range of microwave frequencies these fluctuations are predominantly caused by local inhomogeneities of the water vapor concentration in the atmosphere.

The atmospheric inhomogeneities can be statistically described if the mean correlation length and the mean deviation of the coefficient of absorption and refraction index are known. Direct measurements of the local fluctuations of the refractive index of the atmosphere have shown correlation lengths of the atmospheric inhomogeneities from a few centimeters up to a few kilometers. The rms deviation of the coefficient of absorption and of the refractivity index of an ensemble of inhomogeneities of similar size seems to increase proportionally to the linear dimensions of the inhomogeneities.

Phase and amplitude fluctuations of the electromagnetic wave propagating through an inhomogeneous atmosphere can be conveniently described by introducing the complex phase fluctuation [14].

$$\psi = \phi - i x$$

where: ϕ -real phase fluctuation
 x -logarithm of the amplitude fluctuation
due to atmospheric extinction

The spatial distribution of the complex phase fluctuations depends strongly on the statistical properties of the inhomogeneities. Assuming that the distribution of the correlation lengths is random, locally homogeneous and isotropic, the spatial distribution of the complex phase fluctuations can be adequately described by the structure function defined as

$$(30a) \quad D_{\psi}(r) = | \psi_{(1)} - \psi_{(2)} |^2 ,$$

where \underline{r} is the separation between points 1 and 2.

An analytical expression for the complex structure function can be derived under some simplifying assumptions. Applying the results of turbulence theory to the microwave inhomogeneities in the atmosphere, Tatarski [15] found that at distances comparable to the correlation lengths of the inhomogeneities the structure function can be approximated by

$$(30b) \quad D_{(\psi)}(r) = c_0 r^{5/3} \quad r_0 < r < R_0 .$$

Here r_0 and R_0 are the lower and upper limits of the correlation lengths of the inhomogeneities, respectively. Outside this distance range the structure function can be approximated by:

$$(30c) \quad D_{(\psi)}(r) = C_0 r^2 \quad \text{for } r < r_0$$

and

$$(30d) \quad D_{(\psi)}(r) = \text{constant} \quad \text{for } r > R_0$$

respectively.

The influence of random phase and amplitude fluctuations on the radiation characteristics of single-dish antennas has been extensively treated in literature. Due to the complexity of the equations involved, solutions of this problem have been attempted in two different ways:

- i) Analytical solution under very restrictive initial assumptions
- ii) Numerical solution for some specialized, most interesting cases.

The first approach, tried by Ruina and Angulo [16] and under less severe restrictions by Heidebreder [17], has the advantage that the influence of inhomogeneities of different correlation lengths on the antenna characteristics is clearly separated. A numerical solution to the problem was tried by Mitchell [14]. He gives the results of his computations in the form of diagrams and empirical approximations which are well suited for practical applications. In the following we will discuss analytical and numerical solutions in some detail.

i) Analytical approach.

In most cases of practical importance, one can neglect the influence of the amplitude fluctuations (caused by atmospheric extinction) and assume that the phase fluctuations are small as compared to unity everywhere within the limits of the antenna aperture. [It is convenient for the computation to decompose the phase fluctuations into a linear component defined by the mean instantaneous wave front and a residual random component with the mean value equal to zero.] The direction of the main beam of the antenna at a given time is defined as the direction of the maximum instantaneous received power.

It is shown by Heidbreder [17] that under these assumptions the influence of the phase fluctuations across the antenna aperture can be decomposed into two components: a main beam tilt, determined mainly by phase fluctuations with a correlation length comparable or greater than the antenna aperture; and a main beam broadening, determined by the small scale residual phase fluctuations. The instantaneous direction of the maximum received power or, according to our definition, the direction of the beam tilt, coincides with the normal to the plane wave front. The equations derived by Heidbreder assume an especially simple form in the case of a one-dimensional antenna aperture.

$$(31a) \quad \text{Instantaneous tilt angle } g = \frac{\int_{-\frac{d}{2}}^{+\frac{d}{2}} w(x) x \phi(x) dx}{\int_{-\frac{d}{2}}^{+\frac{d}{2}} x^2 w(x) dx}$$

$$(31b) \quad \text{Variance of the tilt angle } \overline{g^2} = \frac{\int_{-\frac{d}{2}}^{+\frac{d}{2}} \int_{-\frac{d}{2}}^{+\frac{d}{2}} w(x)w(y)xyD(x-y) dx dy}{\left[\int_{-\frac{d}{2}}^{+\frac{d}{2}} x^2 w(x) dx \right]^2}$$

- where: $\phi(x)$ instantaneous phase of the incident wave
 $w(x)$ illuminating weighting function
 $D(x-y)$ phase structure function
 d length of aperture

Adopting for the phase structure function Tatarski's law, e.g. (30b), it can easily be shown that the variance of the beam tilt angle decreases with increasing antenna aperture. On the other hand, the beam broadening increases due to increase of the residual phase fluctuations.

Ruina and Angulo have shown under very restrictive assumptions that the sum of the mean square beam tilt and of the beam broadening remains constant and is equal to the mean square fluctuation of the angle of arrival. This result was found not to depend on the size of the aperture.

It is difficult to derive an analytical expression for the beam broadening in the general case, due to the complexity of the equations involved in such a computation. For inhomogeneities of the atmosphere, whose correlation lengths are small as compared to ^{the} size of the aperture, the rms phase error of a plane wave propagating through this atmosphere is given by [18]

$$(32) \quad \langle \delta^2 \rangle = \frac{4\pi^{5/2} s \ell_0 \langle \Delta n^2 \rangle}{\lambda^2}$$

with s the effective path length through the atmosphere
 l_0 the correlation length
 $\langle \Delta n^2 \rangle$ the mean square fluctuation of the refractive index
 λ the wavelength

This phase error affects the gain of the antenna in the same way as do random reflector deviations. The combined effect of phase fluctuations introduced by both atmosphere and reflector deviations can be described by substituting for $\langle \delta^2 \rangle$ in equations (20) the sum of equation (15) and equation (32). Equation (32) is strictly valid only in the case of a constant correlation length, which is certainly only a very coarse approximation of the true situation. In general one expects the observed effect of atmospheric inhomogeneities on the antenna characteristics to be a superposition of three separate effects:

- α inhomogeneities whose correlation length is larger than the aperture diameter cause mainly a beam tilt
- β inhomogeneities whose correlation length is of the order of the aperture diameter cause a distortion of the main beam
- γ inhomogeneities whose correlation length is small as compared to the aperture diameter decrease the antenna gain and introduce an error pattern in the same way as described in sect. II.a.

In addition the strengths of these effects will also depend on the time over which the observations are averaged.

ii) Numerical approach

Numerical computations were performed by Mitchell [14] for circular and linear antenna apertures. He adopted a phase structure function of the form

$$(33) \quad D_{(\psi)}(r) = b^2 r^\beta$$

Mitchell uses for his numerical computations values of the exponent $\beta = 1, 5/3, 2$. The parameter b gives the rms phase difference between center and edge of the aperture. By comparison with eq. (30 b,d,c) we see that this model should give a good approximation of the phase fluctuations over a wide range of the correlation lengths. Mitchell's computations proceeded from an integral giving the diffraction pattern of an antenna for the case of a partially coherent field. This integral is due to Shore [19].

$$(34) \quad P(u) = \int_0^2 C(r) \gamma(r) J_0(ur) r dr$$

with $C(r)$ the illumination convolution function

$\gamma(r)$ normalized mutual coherence function

$$u = 2\pi \frac{R \sin \theta}{\lambda}$$

R radius of the aperture

Mitchell uses in his computations a gaussian aperture illumination function with an edge taper of 0; 8.6; and 17.2 dB, respectively.

Antenna radiation patterns have been computed for all possible combinations of illumination function and structure function with b as a parameter. It is found for both linear and circular apertures that the main beam is broadened and the gain of the antenna is reduced, and that the side lobe structure is completely blurred even for low levels of the phase fluctuations. For large levels of fluctuations the radiation pattern is practically independent of the illumination function.

In the range of the parameter, $0 < b < 3$, the reduction of the gain normalized to the gain for coherent illumination can be accurately represented by the empirical approximations:

$$(35c) \quad \left[\frac{\Delta G}{db} \right] = 1.37 \cdot b^{1.61} \quad \text{and} \quad \left[\frac{\Delta B}{\%} \right] = 12.1 \cdot b^2$$

For the half-power beam width in the case of the coherent illumination, the value $1.271 \lambda/D$ has been adopted. It should be pointed out, however, that Mitchell derived his equations for an infinite integration time. These equations are therefore upper limits for the beam broadening which we would expect to find with finite integration times. The computed gain reduction and beam broadening (eqs. 35) are due to the combined influence of atmospheric inhomogeneities of various correlation lengths as listed under α , β , and γ .

V. b. Discussion of Methods to Detect Atmospheric Phase Fluctuations

In the experimental investigation of atmospheric effects on the antenna characteristics, the principal difficulty arises from the problem of separating atmospheric and instrumental effects. Random and large-scale reflector deviations

and pointing and tracking errors affect radio astronomical observations in a similar way as do phase and amplitude fluctuations of the ^{atmospheric origin} ~~atmosphere~~. Depending on both the correlation length of the fluctuations and the time interval over which the observations are averaged, the obtained results will differ significantly. Table 4 lists the most prominent observed features as a function of correlation length and averaging time. Also listed are those instrumental effects which tend to obscure mainly the corresponding atmospheric effects.

It is of interest to note that the radio telescope seems to be most "sensitive" (in the sense that observed effects can be unambiguously recognized as of atmospheric origin) to the inhomogeneities whose correlation length is comparable with the size of the antenna aperture. The effects due to the small-scale inhomogeneities are hardly distinguishable from random reflector deviations. On the other hand, the effects due to atmospheric inhomogeneities with large correlation length can erroneously be interpreted as tracking in-often accuracy. This selection effect/causes measured correlation lengths of the atmospheric inhomogeneities to be correlated with the size of the antenna aperture which was used for the observations.

The problem of separating instrumental and atmospheric effects can, in principle, be resolved by using the following characteristics of atmospheric phase fluctuations:

- i) Dependence upon zenith distance. Atmospheric effects can be expected to increase as a function of $\sec z$
(z = zenith distance)
- ii) Dependence upon the water vapor content in the atmosphere.

Table 4

	Large corr. length $r_0 \gg D$	Comparable to the antenna aperture $r_0 \sim D$	Small corr. length $r_0 \ll D$
Short averaging time $t \ll t_0$	Observed effect: Main beam tilt Source of errors: Inaccuracy of pointing and tracking	Observed effect: Main beam distortion Source of errors: Inaccuracy of tracking Large-scale distortion of the reflector	Observed effect: Gain reduction Error pattern Source of errors: Small-scale distortions of the reflector
Long averaging time $t \gg t_0$	Observed effect: Main beam broadening Source of errors: Inaccuracy of pointing and tracking Large-scale distortion of the reflector surface	Observed effect: Main beam broadening Source of errors: Inaccuracy of pointing and tracking Large-scale distortion of the reflector surface	Observed effect: Gain reduction Error pattern Source of errors: Inaccuracy of pointing and tracking Small-scale distortion of the reflector surface

with D the diameter of the antenna aperture
 t_0 correlation time of the fluctuations
 r_0 correlation length of the fluctuations
t averaging time

Meteorological condition can be expected to have a strong influence on atmospheric ~~effects~~. *phase fluctuations*

- iii) Dependence of the observed scintillation on the angular diameter of the source. One can expect that the observed scintillation will be strong for sources whose angular diameter is much smaller than the half-power beam width of the antenna. A necessary condition for the detection of scintillation effects at all is that the beam tilt angle is comparable to the antenna HPBW.

On the other hand, there are, in addition to the effects listed in Table 4, a number of effects which tend to obscure an interpretation of the observational results:

- iv) Change of the antenna characteristics with hour angle and declination.
- v) Change of antenna characteristics with meteorological conditions (temperature, wind velocity).
- vi) Statistical fluctuations due to receiver instabilities, thermal radiation of the atmosphere and inaccuracies of pointing and tracking.

It appears that in this situation the most suitable method for detecting weak atmospheric phase fluctuations in the presence of strong instrumental effects is to investigate the statistical properties of the intensity fluctuations at the output of the receiver under different observing conditions.

Considering the instrumental facilities available at the NRAO for these observations, we decided to investigate the rms value and the power spectrum of the intensity fluctuations as a function of the zenith distance, the weather conditions, and the angular diameter of the source. In order to reduce

the errors caused by the receiver instabilities and the sky noise fluctuations, we used the following on-off procedure: the intensity fluctuations at the radiometer output were investigated with the antenna pointing consecutively on the source and several HPBW's off the source. We assume then that the on-off rate is short as compared to a noticeable change in the statistical characteristics of both the sky noise fluctuations and receiver gain. Hence their contribution to rms value and power spectrum should cancel if only differences are considered.

V. c. Observations and Data Reduction

The observations discussed here were made at $\lambda = 2$ cm during the OP VII. A few additional observations also included in this report have been made on May 5 at $\lambda = 18$ cm. The following test sources were used: 3C 84 and 3C 273 which have a very small angular diameter; the extended source M 17; and Virgo A, which has a HPW of somewhat less than one minute arc. The total observations consist of 74 on-off measurements corresponding to a total of 14.5 hours of actual observing time. In order to assure accurate pointing and focusing of the antenna, pointing and focusing corrections were carefully determined (and adjusted if necessary) before each on measurement. Immediately after an on measurement, the antenna was pointed off the source by five to ten beam widths in right ascension, and the measurement of the fluctuations was repeated. In order to reduce influence of the sky noise, the switched beam technique was used through the whole observation period (see J.W.M. Baars [20]).

The observations were made in the gaps between other test measurements, predominantly when the weather conditions were considered to be unsuitable for other tests. About half of the observations were made during

rain or snowfall with wind velocities over 10 m.p.h.; one-third of all measurements have been made during clear and calm weather. The observing conditions during the remaining part of the observations were fair.

An on- or off-measurement lasted about six minutes. During these six minutes 250 digital samples of the receiver output were recorded with an integration time of one second and a sampling rate of 1.44 second. The digital records were used to compute the rms value of the amplitude fluctuations, the autocorrelation function and the power spectrum, using the IBM 7040 NRAO computer. In the data reduction the running mean was subtracted from the data points and the amplitudes of the remaining fluctuations were normalized with respect to the antenna temperature of the source. In this way the effects caused by gain variations of the telescope were removed in the first approximation. The power spectrum was computed proceeding along lines suggested by Blackman and Tukey [21].

In the first step, the autocovariance function was computed according to the formula:

$$(36) \quad A(n\Delta\tau) = \frac{1}{N-n} \sum_{k=1}^{N-n} x_k \cdot x_{k+n}$$

with x_k the normalized sample of the receiver output
 $\Delta\tau$ the sampling interval
 N the total number of samples
 $0 \leq n \leq K$
 $n = \text{integers}$

The maximum time lag used for the computation of the autocovariance function was $K = 25$ sampling intervals or 36 seconds. The rms value of the fluctuations of x was computed from

$$(37) \quad \langle x^2 \rangle_{\text{rms}} = \sqrt{A(0)}$$

The Fourier transform of the autocovariance function yields the power spectrum:

$$(38) \quad P\left(\frac{n}{2\Delta T N}\right) = 2\Delta T A(0) + 4\Delta T \sum_{k=1}^K A(k\Delta T) w(k\Delta T) \cos \frac{\pi n k}{N}$$

$$0 \leq n \leq K \text{ integer}$$

With $w(k\Delta T)$ the weighting function, for which we adopted

$$(39) \quad w(n\Delta T) = 0.42 + 0.50 \cos \frac{\pi n}{N} + 0.08 \cos \frac{2\pi n}{N}$$

This weighting function (the so-called Blackman spectral window) was used since it gives a very low spurious spectral response. The lower frequency resolution obtained by using this weighting function is in our case not a serious disadvantage.

The lowest recovered frequency, as well as the spectral resolution, was 0.0139 Hz; the highest recovered frequency was 0.347 Hz. Thus each spectrum consists of the 25 independent points.

For each on- and off-measurement the rms value, the autocorrelation function and the power spectrum of the fluctuations were computed. Along with

those quantities the on-off difference of the rms value and power spectrum, as well as the ~~secans~~^{secant} of the mean zenith angle z were computed. Fig. 21 shows the difference between the rms value computed for on-source and off-source observations. The fluctuations observed during the on-source observations are significantly greater. The points in Fig. 21 are plotted as a function of $\sec z$. Different sources are characterized by different symbols. It was found (but is not shown in this diagram) that the difference in the rms fluctuations seemed to be larger for observations made during winds over 15 m.p.h. There is no obvious correlation between the points plotted in Fig. 21 and the relative humidity (water vapor content of the atmosphere) or source size (scintillation), although observations are too scarce to obtain conclusive results. The investigation of the power spectra reveals some interesting characteristics of the intensity fluctuations. Fig. 22 shows as a typical example the power spectrum (eq. (38)) computed from observations of 3C 273, which were made during excellent observing conditions at two different elevation angles. In both cases--as well as in the majority of all investigated spectra--the on-source spectrum shows a significant increase at the low-frequency end. During winds above 15 m.p.h. the power spectra show in few cases remarkable structure. The most interesting example of such spectra is plotted in Fig. 23. Again we see the increase at the low-frequency end; but, in addition, there are two other peaks whose center frequencies appear to be harmonically related.

V. d. Interpretation of Observational Results

In view of the very limited amount of data which was obtained during the testing period (mainly OP VII), we want to restate the preliminary and tentative nature of the interpretation which we try to give in the following. The

difficulty in the interpretation arises from two facts: i) We have a limited number of measurements which show a large variety of features. ii) In nearly every case an observed feature can be explained as being either caused by the instrument or caused by the atmosphere.

We consider the most appropriate way to deal with this problem is to list first the most obvious features which we obtained by evaluating the observations. We then try to interpret these features as being caused by atmospheric effects and list those observed features which either support or disprove this explanation. Then we proceed in the same way explaining the results as being caused by the instrument.

- i) The rms value of the fluctuations on source is systematically greater than the rms fluctuations off the source. Typical differences are about $0.5 \div 1.5\%$ of the total flux of the source at elevation angles above 25° . This difference then increases rapidly to about 6% at elevation angles around 10° .
- ii) Both on and off rms fluctuations increase roughly linearly with secant z .
- iii) Rms fluctuations on source seem to be systematically larger for observations during winds above 10 m.p.h.
- iv) There is no significant increase in the rms fluctuations during moderate rain or snowfall.
- v) There is no significant correlation of the observed rms fluctuations with the angular diameter of the source.
- vi) There is no significant difference between on and off rms fluctuations measured at $\lambda = 18$ cm. (However, only four measurements were made.)
- vii) The power spectra show significant increase toward the low frequency end. This effect is the stronger the larger

the zenith distance, but it is not significantly correlated with weather conditions.

- viii) Only at low elevation angles and during winds above 10 m.p.h. the power spectra show subsidiary maxima which seem to be harmonically related.

The atmospherical interpretation is strongly supported by i) and ii). The features iii), vi) and vii) do not strongly contradict this interpretation. Features listed under iv), v) and viii) are in evident disagreement with this interpretation.

The instrumental interpretation is supported by the features iii), iv), viii). Feature i) can be easily explained as an effect caused by short-term tracking errors of the telescope of the order of 5 seconds of arc (5") close to zenith and under favorable weather conditions. But it is difficult to explain why this tracking error should increase to about 30" of arc at low elevations. The first value is in good agreement with measurements of the short-term pointing error at $\lambda = 0.95$ cm which yielded $\pm 5''$ of arc during excellent weather conditions (and about 20" during the wind up to 20 m.p.h.). The feature listed under viii) shows that at low elevation angles and winds above 10 to 15 m.p.h. the telescope has a tendency to oscillate with characteristic periods of the first harmonics around 8 ± 3 sec. The feature vii) can be explained as a consequence of the decrease in antenna gain with increasing zenith distance (sect. II, c). The observed gain variation is adequate to explain quantitatively the observed low-frequency peak of the power spectra. The feature vi) does not disprove this interpretation. The tracking error of the order 5" to 10" of arc is too small to be detected with the 18' antenna

beam at this frequency. The feature listed under ii) seems to disprove the instrumental interpretation. It should be pointed out, however, that in the adopted normalization procedure the decrease of the antenna temperature of the source (caused by decrease in telescope gain and increase in the atmospheric extinction) will produce an increase of the rms value of the off fluctuations which is inversely proportional to the antenna gain. This increase varies nearly linearly with the secant of the zenith angle because the gain of the telescope changes with zenith distance roughly as $\cos(z)$.

V. e. Conclusions

In this subsection we try to formulate some conclusions relating to a possible influence of the atmosphere on the characteristics of the 140-foot telescope. In addition to the results discussed in sect. V, we shall also refer to some results discussed in other sections of this report which may be related to this subject.

Aperture and beam efficiency

In sect. II, c., we mentioned that at $\lambda = 1.95$ cm the aperture efficiency of the 140-foot telescope decreases to less than 50 percent of its zenith value at $z = 80^\circ$. On the other hand, the beam efficiency remains constant over a large range of zenith distances (see Fig. 8). This effect can only be partly explained by the compensating effect of the error pattern (sect. II, a). If this effect were due to atmospheric scintillation, we would expect an increase in the HPW of the main beam with increasing zenith distance. Preliminary observations do not show such an effect, although the amount of observational data is small and the precision of the measurements is not very high.

Angular resolution

Down to a wavelength of 1.95 cm the measured HPBW of the 140-foot telescope agrees with the theoretical values of the diffraction pattern (Table 2). At $\lambda = 0.95$ cm the observed HPBW in α corresponds to the theoretical value; that observed in δ is about 35 percent larger. There are strong indications, however, that this beam broadening is due to a large-scale deflection of the 140-foot reflector (sect. II, h.).

As mentioned above, our measurements of the HPBW at $\lambda = 1.95$ cm as a function of both zenith distance and meteorological conditions are not yet sufficient to yield a quantitative result. There might be, however, a more fundamental reason that we cannot detect such a beam broadening, viz. if the correlation time of the atmospheric scintillation is long as compared to the time which it takes to measure a cross-section through the main beam.

On the other hand, it takes approximately half an hour to obtain a map of the main beam whose integration in turn yields the main beam efficiency. If this time is long as compared to the correlation time of the atmospheric scintillation, the net result would be a blurring of the map, which however will not change the value of the integral $\int T_A d\Omega$.

Pointing and tracking errors.

We discriminate between "short-term pointing errors" (referring to an observing time of several hours) and "long-term pointing errors" (referring to an observing period of a few days or longer).

Several independent tests agreed that with wind speeds below 10 m.p.h. the pointing accuracy of the 140-foot telescope is about 5 seconds of arc (sect. III, c.).

The long-term pointing errors--again measured by independent methods--yield values of the order of about 20 to 30 seconds of arc. Although a dependence of the atmospheric refraction index on meteorological conditions is anticipated, the observational evidence given in sect. III, d. does not support a correlation between temperature and amount of precipitable water and long-term pointing errors.

On the other hand, the results discussed in sect. V show that the pointing accuracy of the telescope impairs at wind velocities above 15 m.p.h. We feel, however, that this is due to instrumental effects rather than due to an increased atmospheric scintillation.

As a concluding remark to this section, it seems appropriate to note that we obviously have not reached the limit imposed by atmospheric scintillations to observations with the 140-foot telescope, at least not at wavelengths as short as 1.95 cm.

REFERENCES

1. Small, M. M. (1965). Sky and Telescope, 30.
2. Horne, W. G. and Small, M. M. (1966). Paper presented at the Plant Engineer and Maintenance Conference, Charleston, W. Va. (available as ASME publication).
3. Wade, C. M. NRAO Internal Report (in preparation).
4. Preliminary Proposal Specification for Design and Fabrication of Antenna Feed Mounting System for the 140-foot Telescope.
5. General Dynamics-Electric Boat Operation and Maintenance Manual Drives and Control System, Vol. I.
6. Mezger, P. G. (1964). An Experimental Check of Antenna Tolerance Theory Using Radio Astronomy Techniques. NRAO Internal Report.
7. Baars, J.W.M. and Mezger, P. G. (1964). NRAO Electronics Division Internal Report 36.
8. Baars, J.W.M., Mezger, P. G. and Wendker, H. (1965). Ap.J. 142, 122.
9. Ruze, J. "Physical Limitations on Antennas", Tech. Report 248, Res. Lab. of Electronics, MIT, October 1952.
10. ---- Proc. IEEE, 54, 633 (1966).
11. Mezger, P. G. (1966). Application of Antenna Tolerance Theory to the NRAO 85-foot and 300-foot Telescopes. Electronics Division Internal Report.
12. Baars, J.W.M. and Mezger, P. G. (1966). Sky and Telescope, 31, 7.
13. Pauliny-Toth, I.I.K. and Kellermann, K. I. "Variations in the Radio Frequency Spectrum of 3C 84, 3C 273, 3C 275 and other Radio Sources". Submitted for publication.

14. Mitchell, R. L. (1966). IEEE Trans. on Antennas and Propagation, 14, 324.
15. Tatarski, V. I. (1961). Wave Propagation in a Turbulent Medium, New York, McGraw-Hill.
16. Angulo, C. M. and Ruina, J. P. (1963). IEEE Trans. on Antennas and Propagation, 11, 153.
17. Heidbreder, G. R. Aerospace Corporation, El Segundo, California, U.S.A.F. Contract No. AF 04(695) - 669.
18. Chandrasekhar, S. (1952). M.N. 112, 475.
19. Shore, R. A. (1963). International Series of Monographs on Electromagnetic Waves. Vol. 6. E. C. Jordan, Ed. New York: Macmillan pp. 787-795.
20. Baars, J.W.M. (1966). Reduction of Sky Noise Fluctuations by Switched Beams Observing Technique. Paper presented at URSI Spring Meeting, Washington, D. C.
21. Blackman, R. B. and Tukey, J. W. (1958). The Measurement of Power Spectra. Dover Publications, Inc., New York.

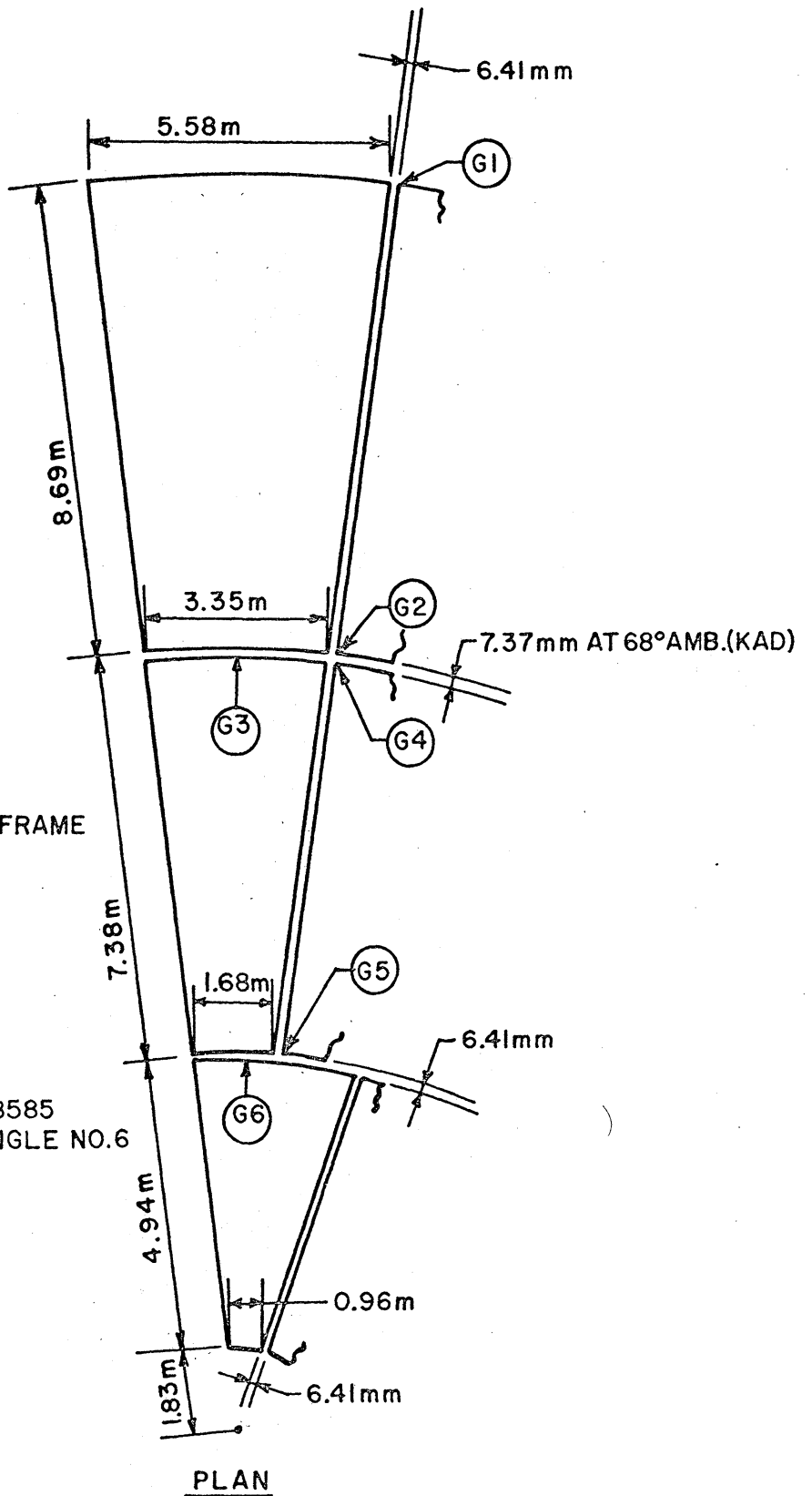
CAPTIONS

- Figure 1a: Size of the panels of the 140-foot reflector
- Figure 1b: Dimensions of the 140-foot reflector and feed support
- Figure 2: The Sterling mount of the 140-foot telescope, which allows a remotely controlled change of axial focus position and polarization angle of the feed
- Figure 3: Dimensions of feed support and support legs
- Figure 4: A drift curve through the sun (Fig. a) is used to determine the main beam (curve b) and the error pattern (curve c) of the 140-foot telescope at the wavelength 9.5 mm
- Figure 5a: Change of aperture efficiency (curve a), main beam efficiency (curve b) and measuring beam efficiency (curve c) with axial focus position
- Figure 5b: Change of main beam HPBW of the 140-foot telescope in one principal plane with axial focus position
- Figure 6: Decrease of gain and increase of the "coma" lobe computed for the F/D ratio of the 140-foot telescope as a function of lateral feed displacement by J.W.M. Baars. Parameter is the edge taper of the feed pattern
- Figure 7: Relative change of "aperture" efficiency as a function of hour angle. Since observations have been made with extended sources, the observed decrease lies somewhere between the decrease of aperture efficiency and that of the main beam efficiency

- Figure 8: Change of aperture efficiency (curves a, b and c) and beam efficiency (curve d) of the 140-foot telescope as a function of zenith distance
- Figure 9a: Change of focal length with hour angle at three different declinations
- Figure 9b: Corresponding change of aperture efficiency
- Figure 10: Change of focal length with declination and hour angle, respectively
- Figure 11a: Change of maximum antenna temperature as a function of rotation angle of the Sterling mount, measured with the feed off-set by 3 HPBW
- Figure 11b: Position of feed, beam, electrical axis and rotation axis and definition of feed angle ϕ_f
- Figure 11c: Change of aperture efficiency (T_A) as a function of lateral feed displacement as computed by J.W.M. Baars. Computed ratio $T_A(\text{min})/T_A(\text{max})$ of the observed change of T_A (Fig. 11a) as a function of the angular displacement $\Delta\theta$ between electrical axis and rotation axis of the Sterling mount. The feed-horn off-set is assumed to be 3 HPBW in this computation.
- Figure 12a: Change of measuring beam efficiency at 9.5 mm wavelength as a function of declination
- Figure 12b: Computed change of measuring beam efficiency as a function of the rms phase error $\langle\delta^2\rangle_{\text{rms}}$ introduced by a random reflector deviation $\langle d^2\rangle_{\text{rms}}$. Parameter is the HPW of the error pattern θ_E

- Figure 13a: Shape of the main beam of the 140-foot telescope in the two principal planes of the antenna as a function of hour angle. Measurements have been made for optimum focal length
- Figure 13b: Contour map of the main beam of the 140-foot telescope at the meridian ^{and} at 4^h 15^m east
- Figure 14: Shape of the main beam of the 140-foot telescope measured in the two principal planes of the antenna at different focal lengths. The position of optimum focal length can be approximately taken from Fig. 9b
- Figure 15a: Axial focusing curves measured at various hour angles with Virgo A
- Figure 15b: Same measurements as Fig. 15a, but using Venus
- Figure 16a: Declination pointing corrections at the meridian, measured at $\lambda = 11$ cm
- Figure 16b: Declination correction at the meridian, measured at $\lambda = 1.95$ cm
- Figure 17: Daily pointing corrections measured at transit with 3C 84 and 3C 273
- Figure 18: Apparent position of 3C 84 as a function of polarization angle of the Sterling mount. The figures attached to the measured points give the indicated polarization angle of the Sterling mount.
- Figure 19: Change of indicated focal length with ambient temperature, measured around transit. The transit time of 3C 84 was approximately at 15^h EST, that of 3C 273 at 0^h EST

- Figure 20: Change of indicated focal length, measured with 4 radio sources as a function of hour angle and ambient temperature
- Figure 21: Difference in the observed rms fluctuations measured on and off a radio source, respectively. The measurements have been obtained with different radio sources and are plotted as a function of the secant of the zenith distance z .
- Figure 22: Power spectra of the radiometer output fluctuations, observed on and off source, respectively. The two spectra have been obtained at different elevation angles but under excellent observing conditions.
- Figure 23: Observed power spectra similar to those given in Fig. 22 but with wind speeds up to 15 mph



MAT'L THICKNESS = 0.125"
 ~ 3.18mm

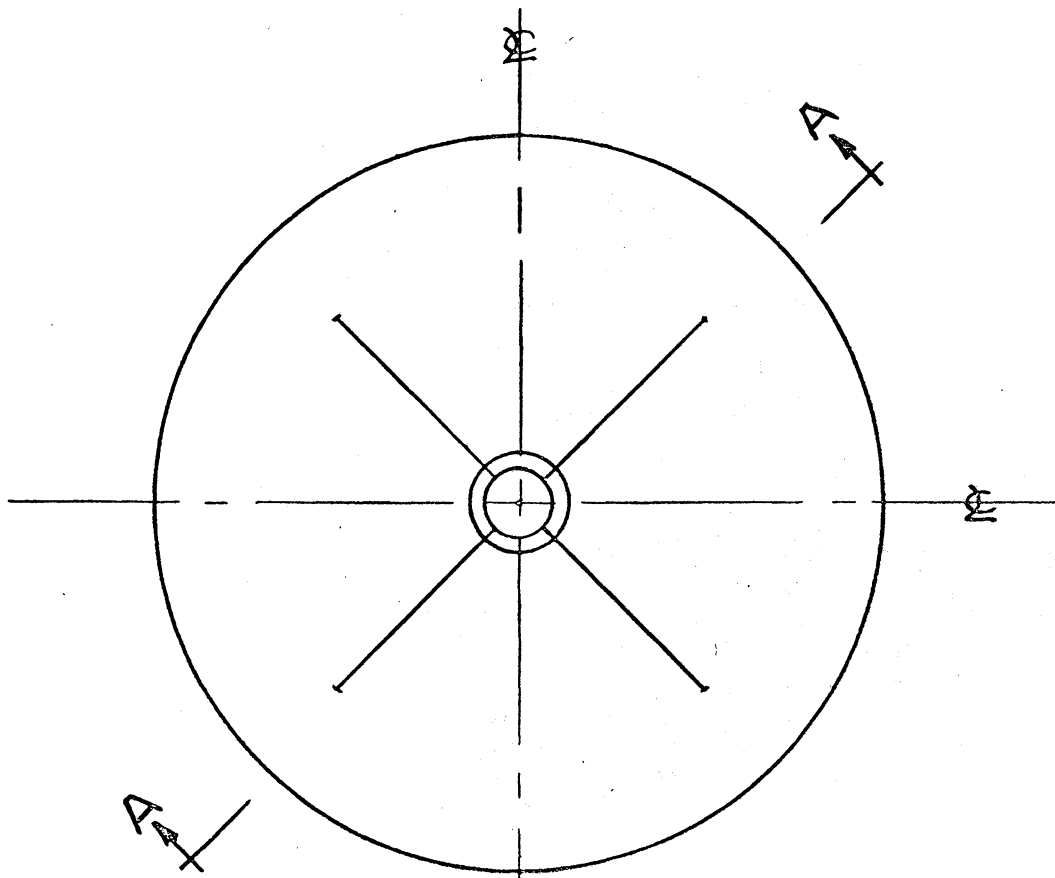
ALLOY: 6061-T6
 SURFACE PLATE & SUPPORT FRAME

PAINT SPEC:

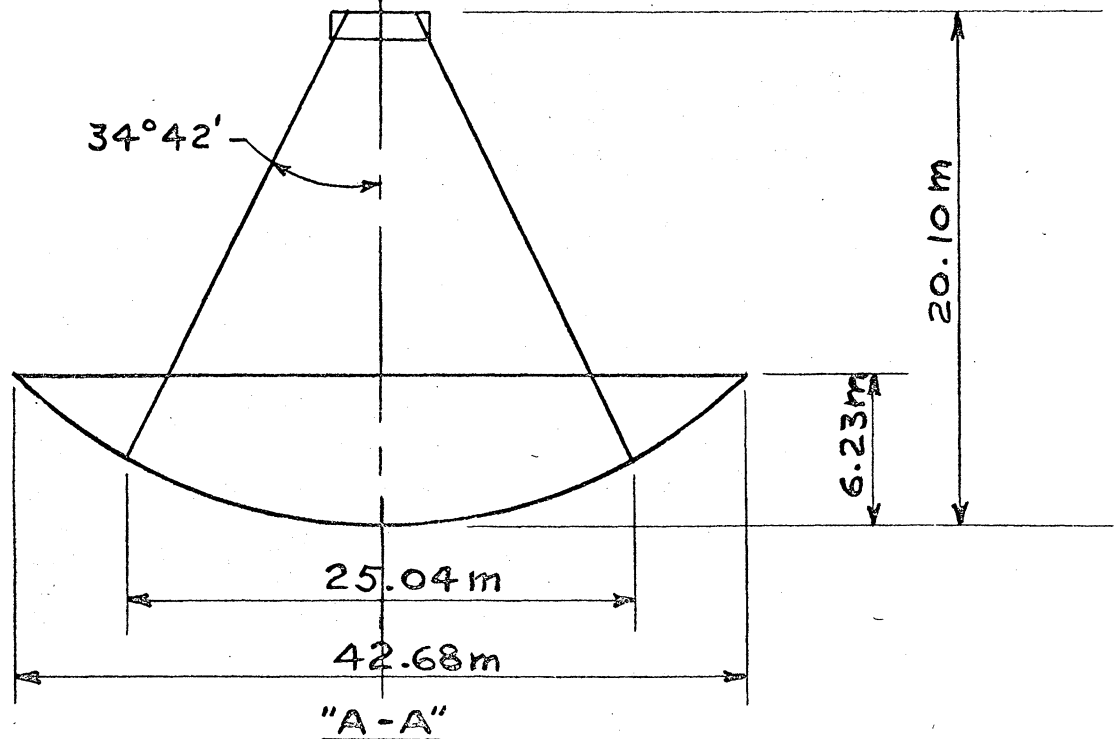
WET WASH PRIMER TO MIL C 8514
 ZINC CHROMATE PRIMER TO MIL P 8585
 2 COATS TRIANGLE PAINT CO. TRIANGLE NO.6

140' TELESCOPE PANELS (60 TOTAL)

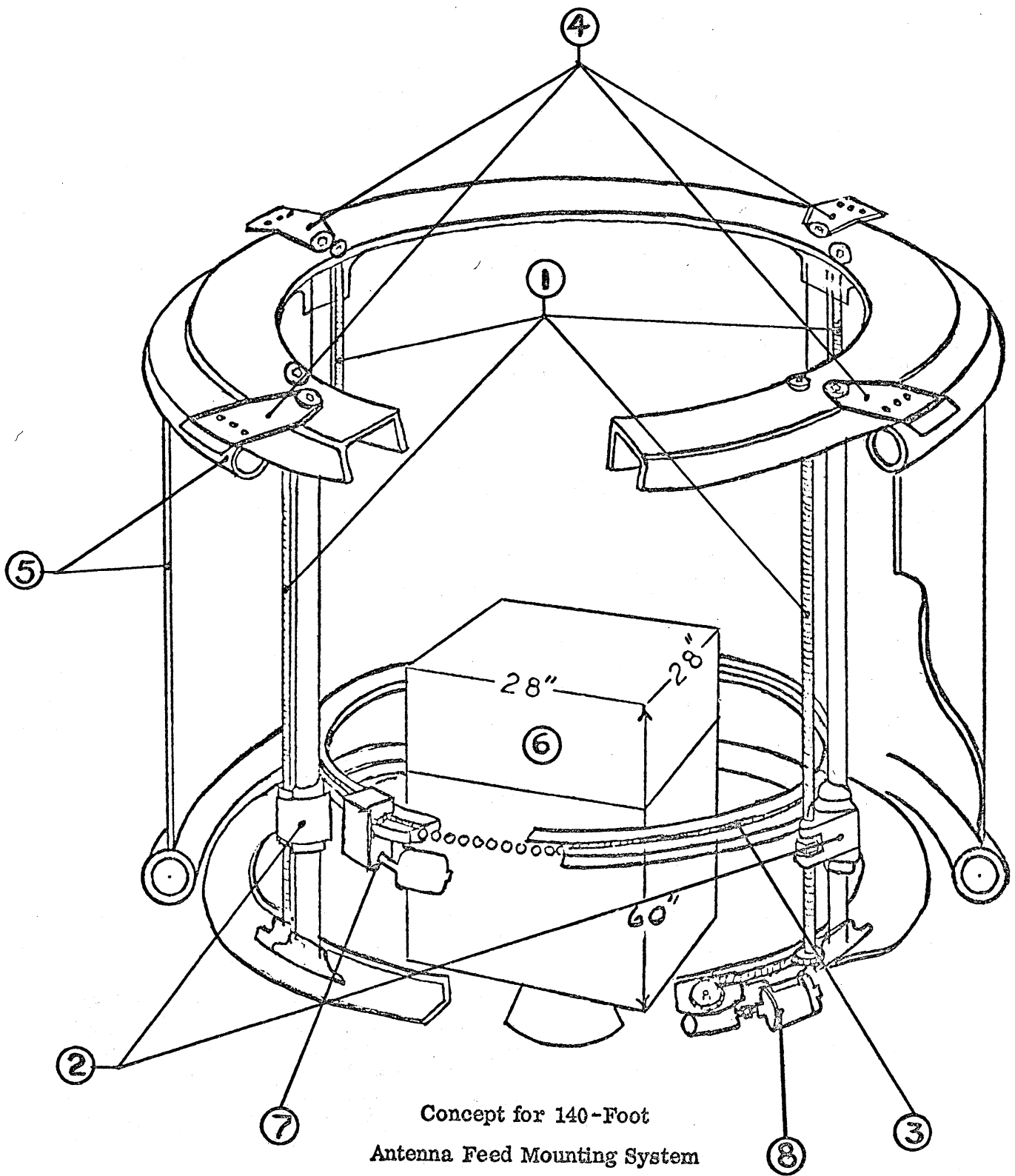
FIG. 1A



PLAN

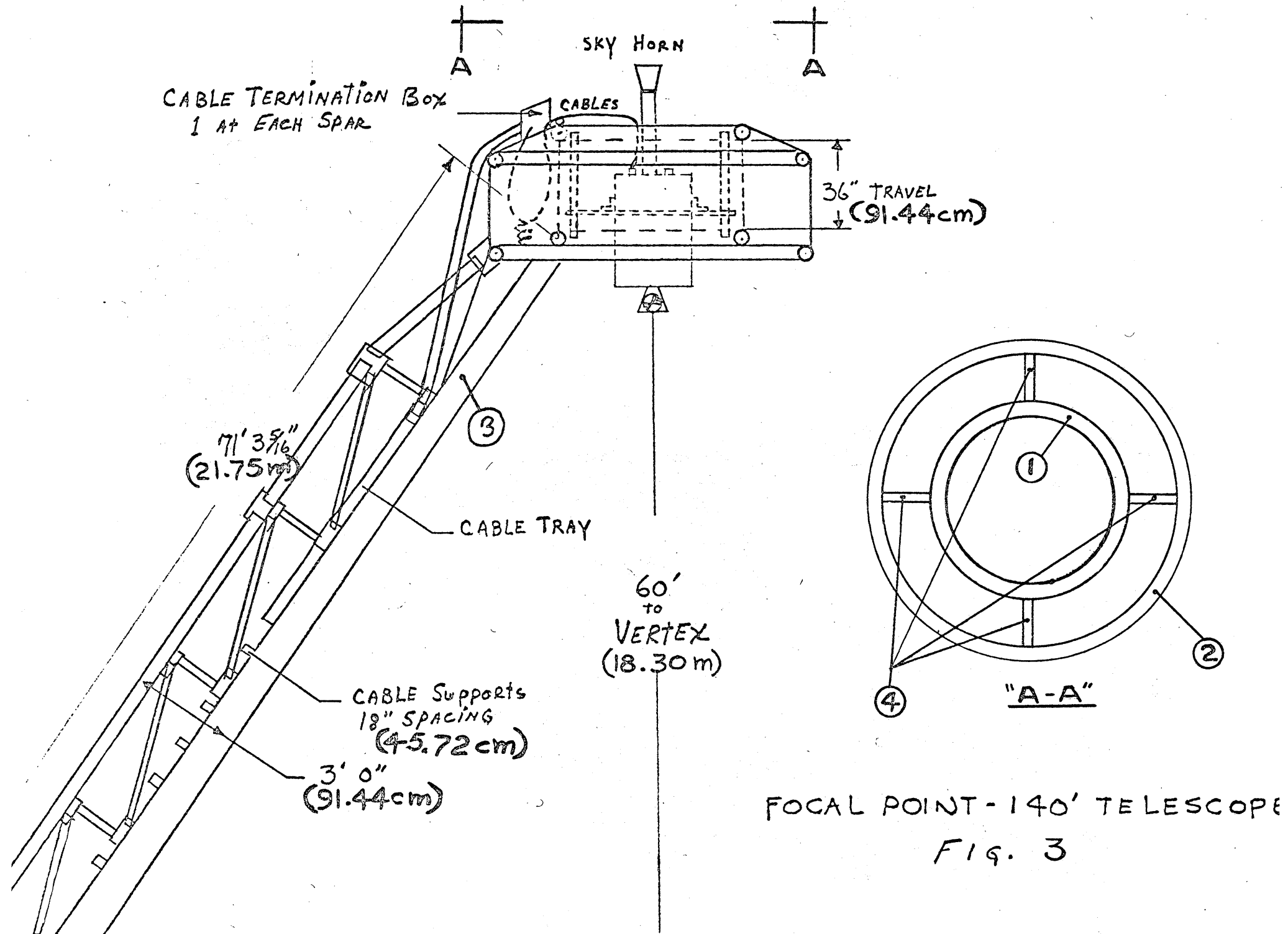


"A-A"

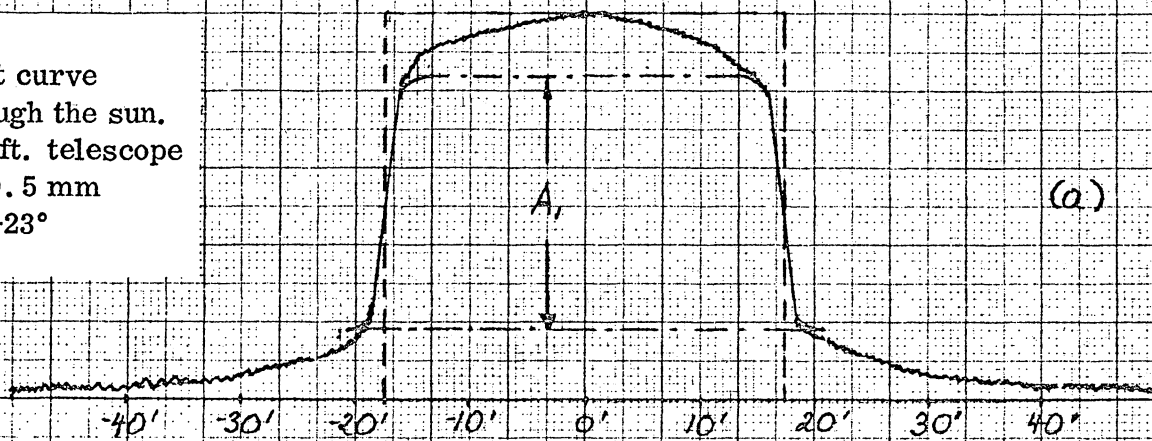


Concept for 140-Foot
Antenna Feed Mounting System

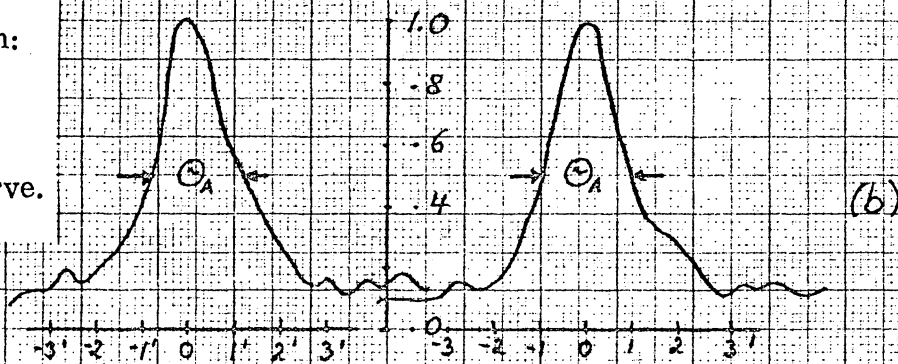
Fig. 2



Drift curve
through the sun.
140-ft. telescope
 $\lambda = 9.5 \text{ mm}$
 $\delta = -23^\circ$



Main beam pattern:
Computed as the
derivative of the
step part of the
observed drift curve.



Error pattern:
Obtained from the
observed drift
curve by subtract-
ing the contribu-
tion
due to the main
beam.

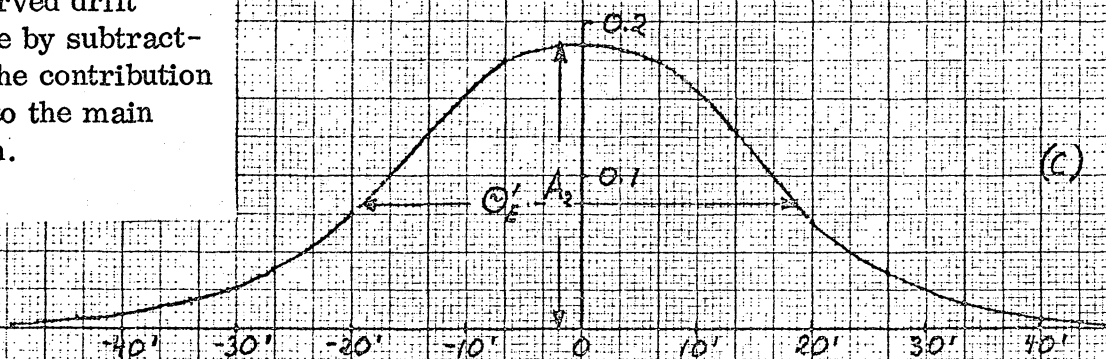
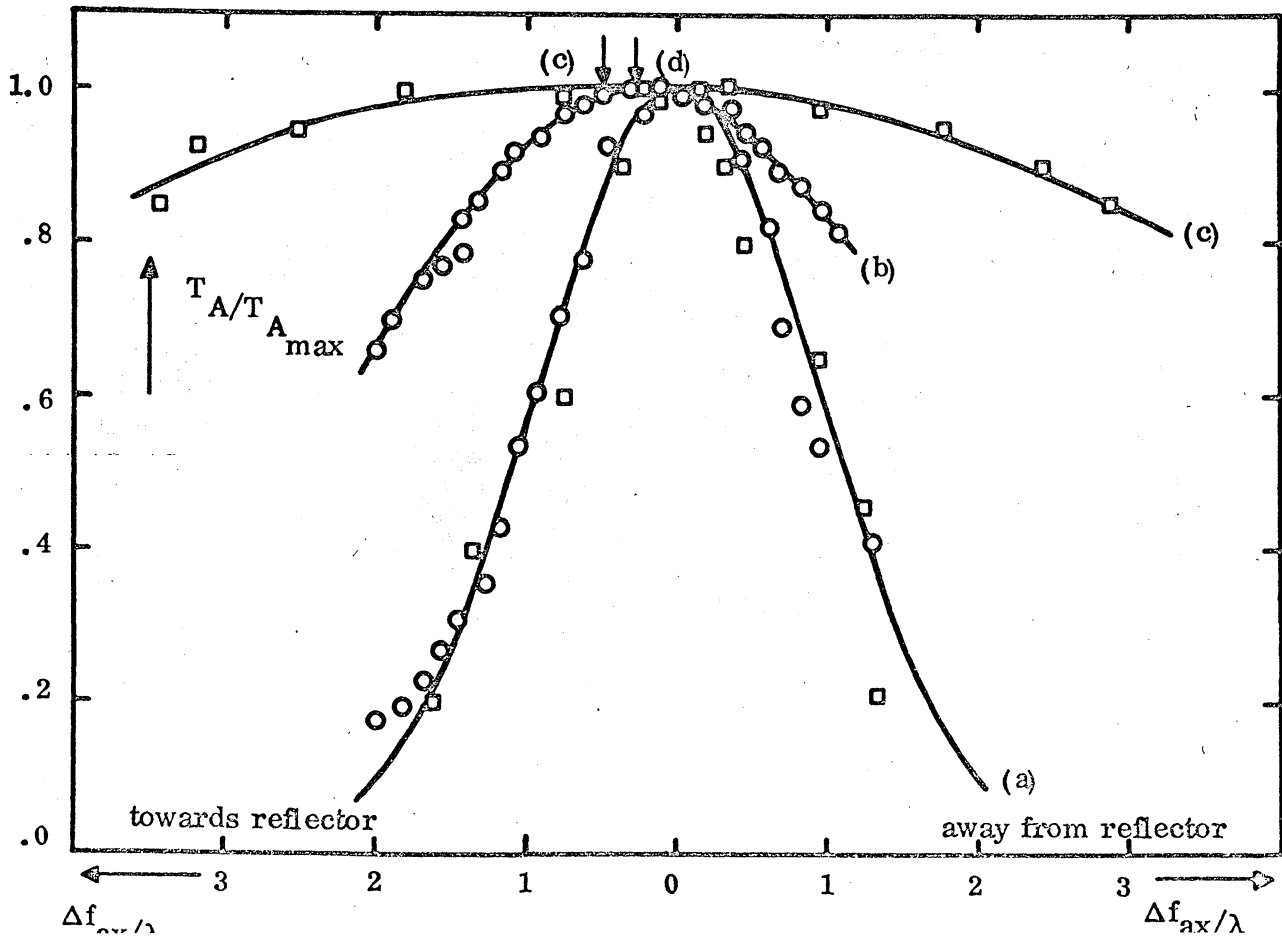
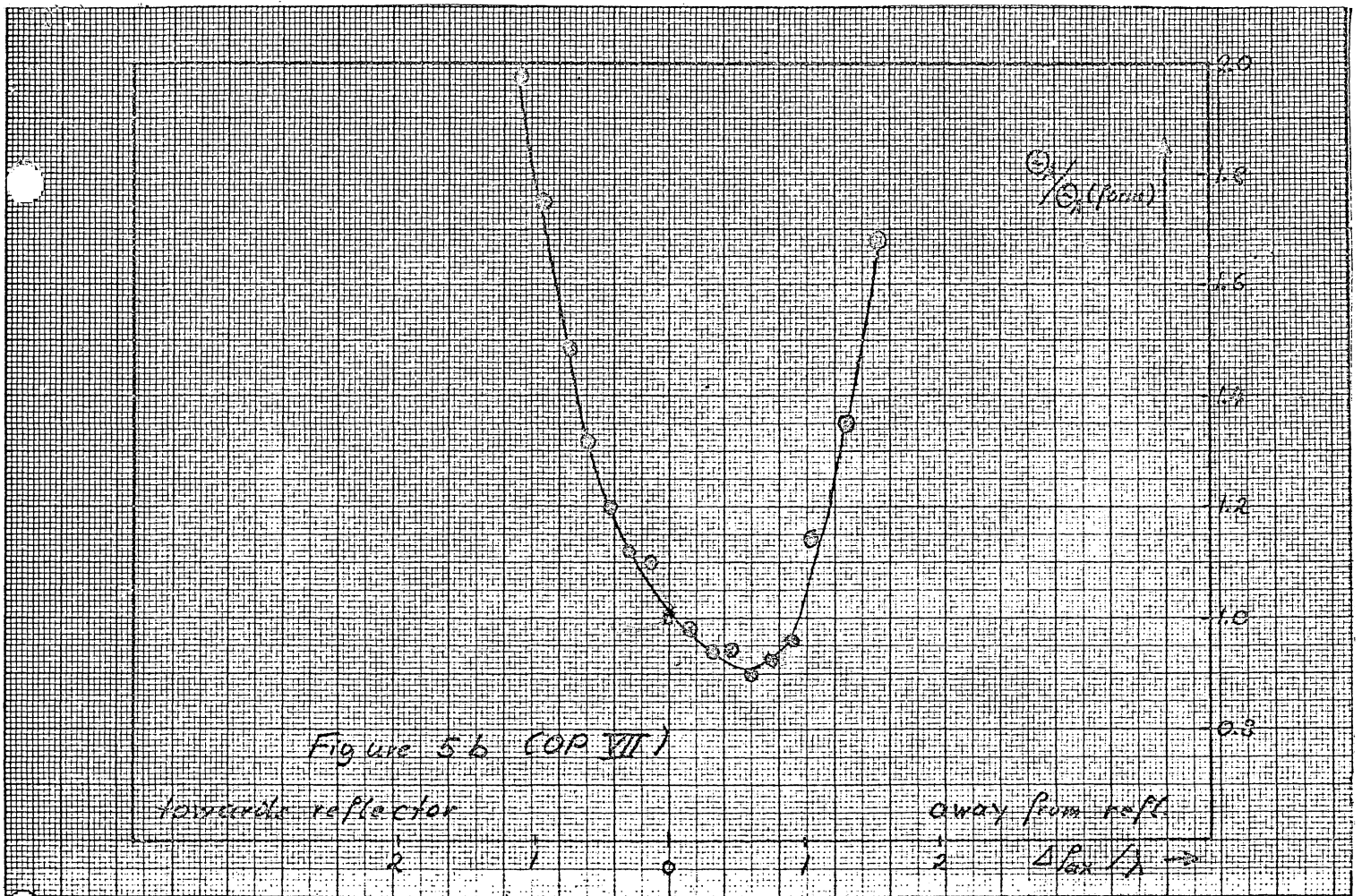


Figure 4 (OP V)



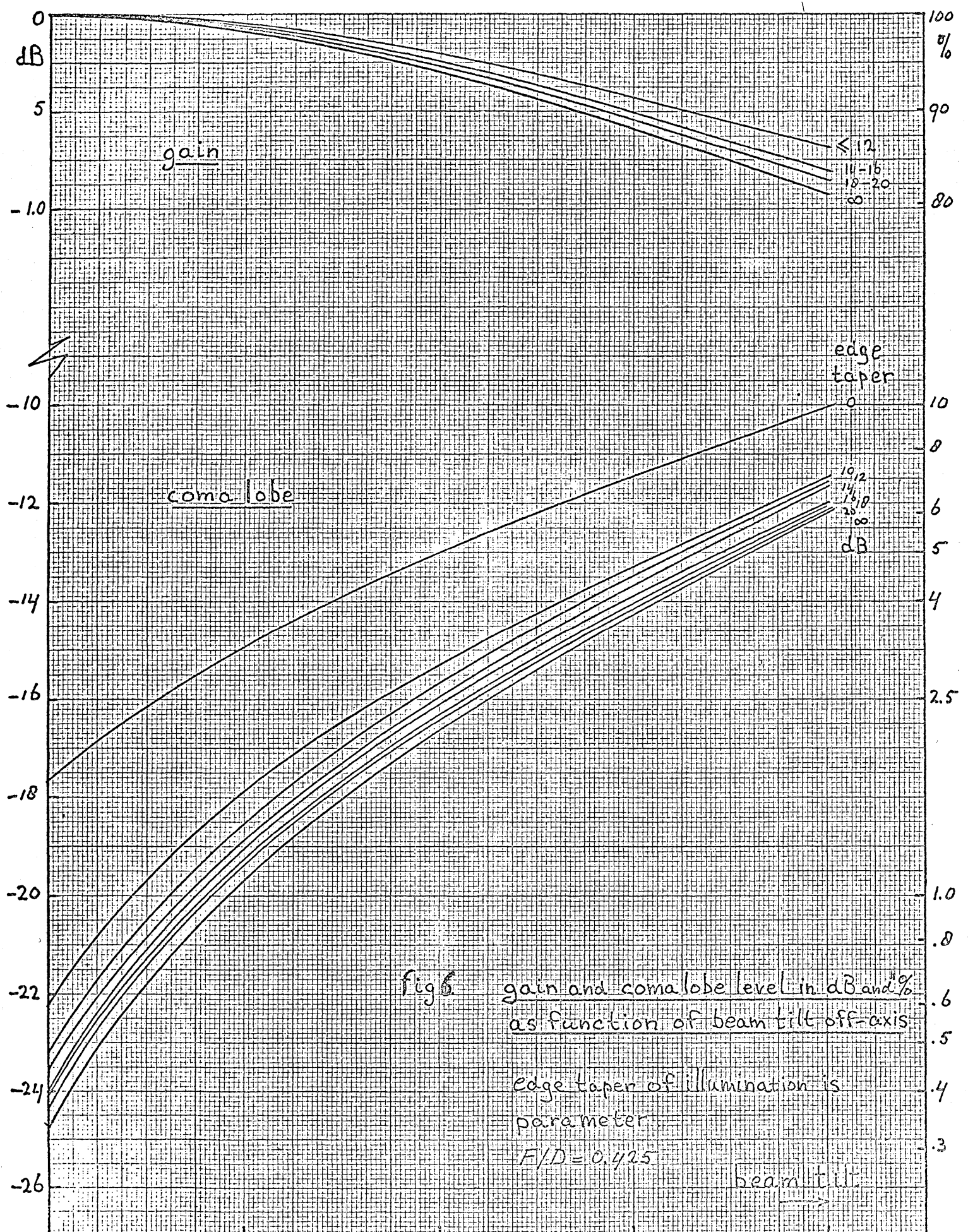


fig 6 gain and coma lobe level in dB and % as function of beam tilt off-axis

Edge taper of illumination is parameter

$F/D = 0.425$

beam tilt

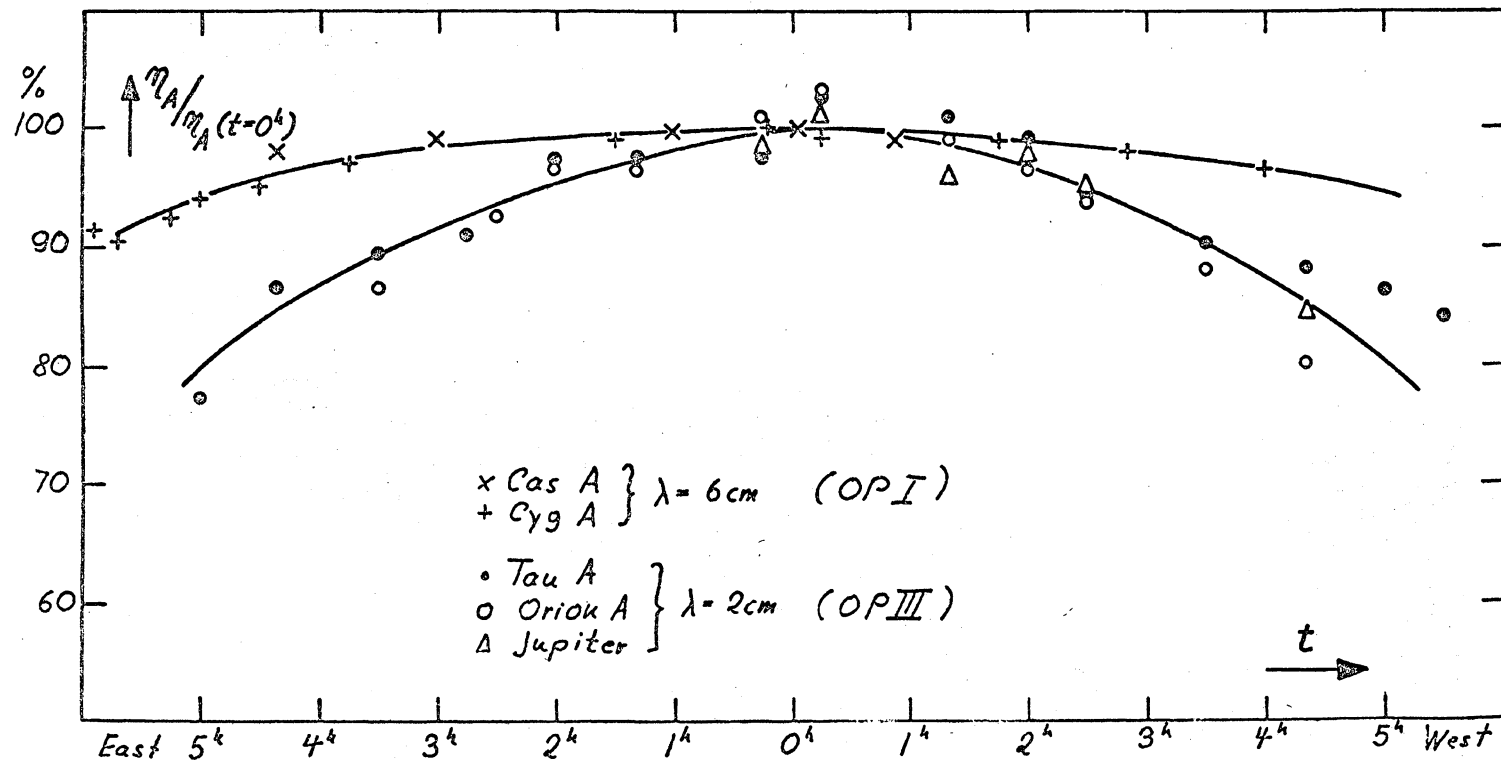


Figure 7

NRAO 140-foot telescope: Relative change of aperture efficiency as a function of hour angle, measured at $\lambda = 6 \text{ cm}$ and $\lambda = 2 \text{ cm}$.

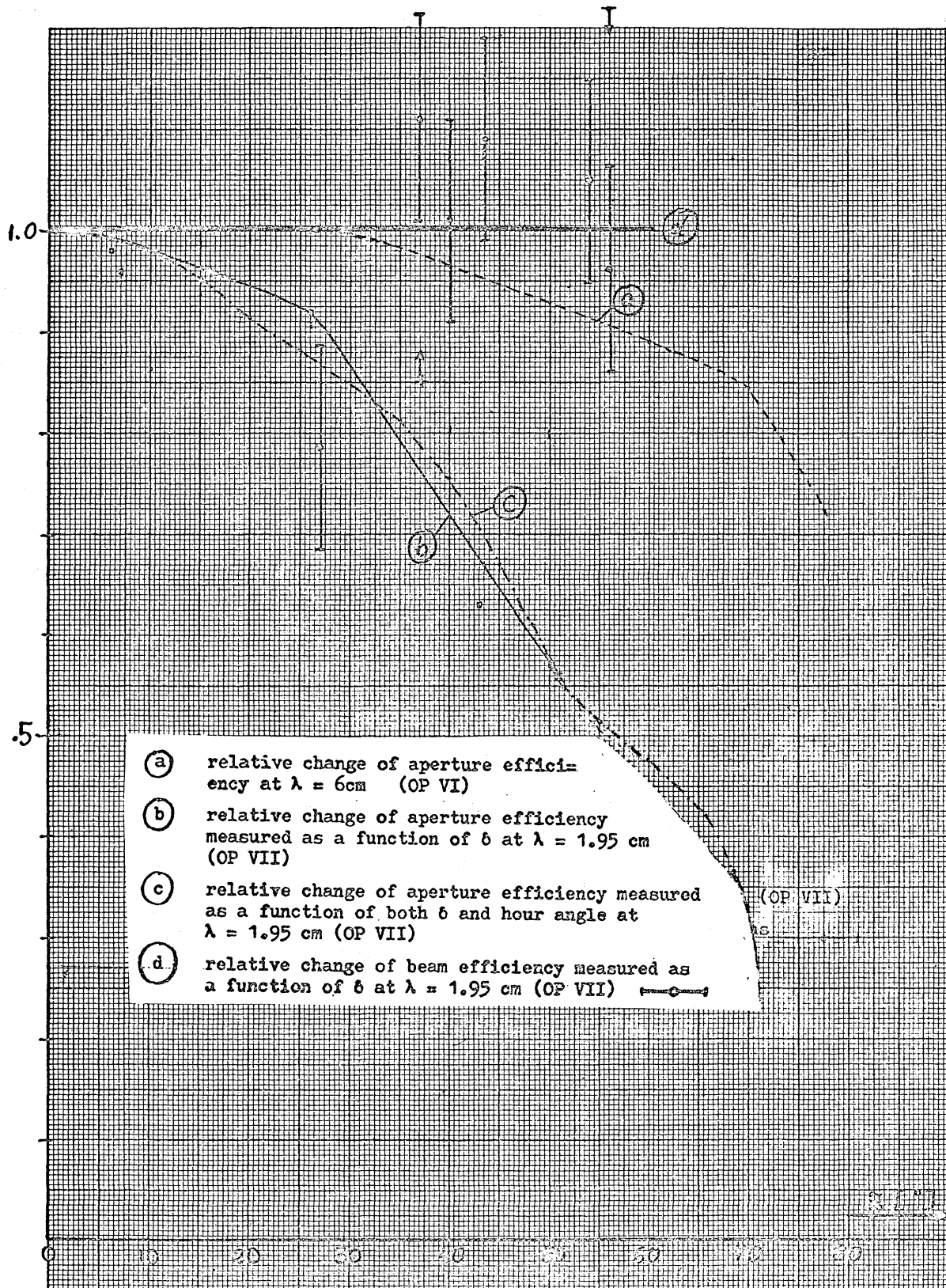


Figure 8

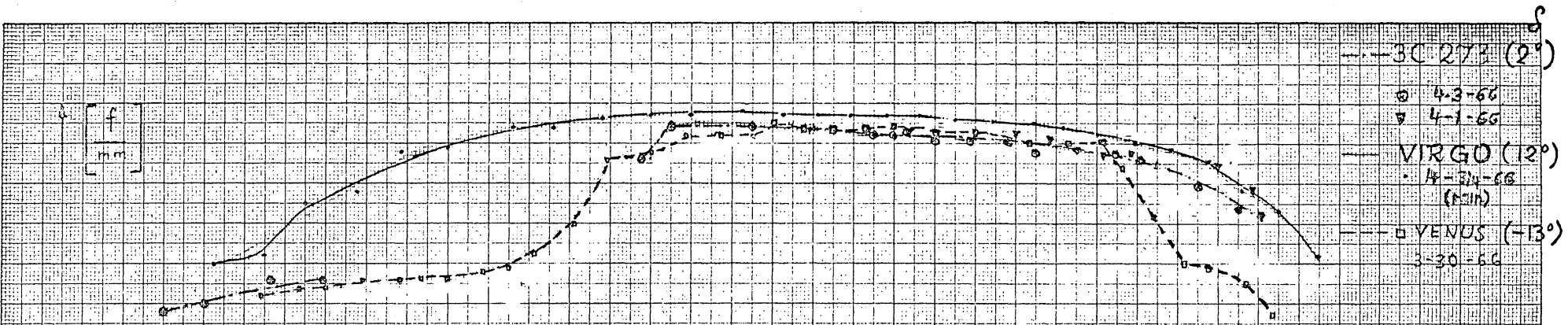


Figure 9a (OP VII)

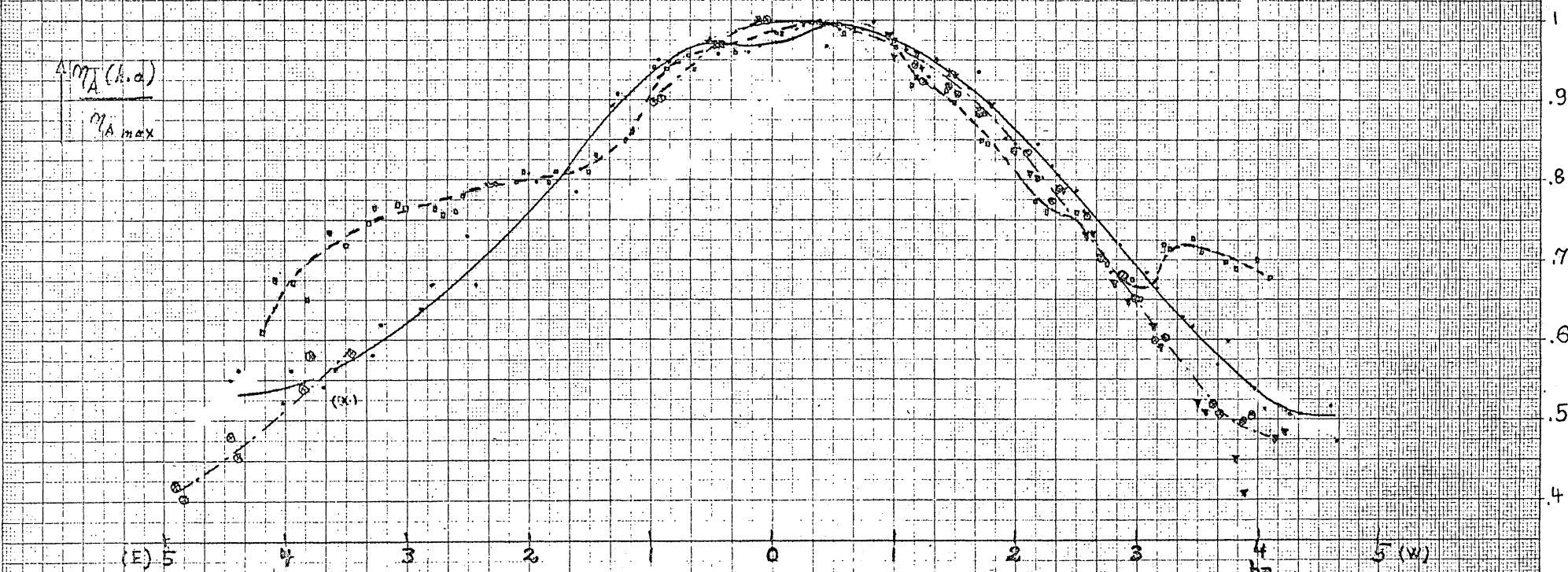
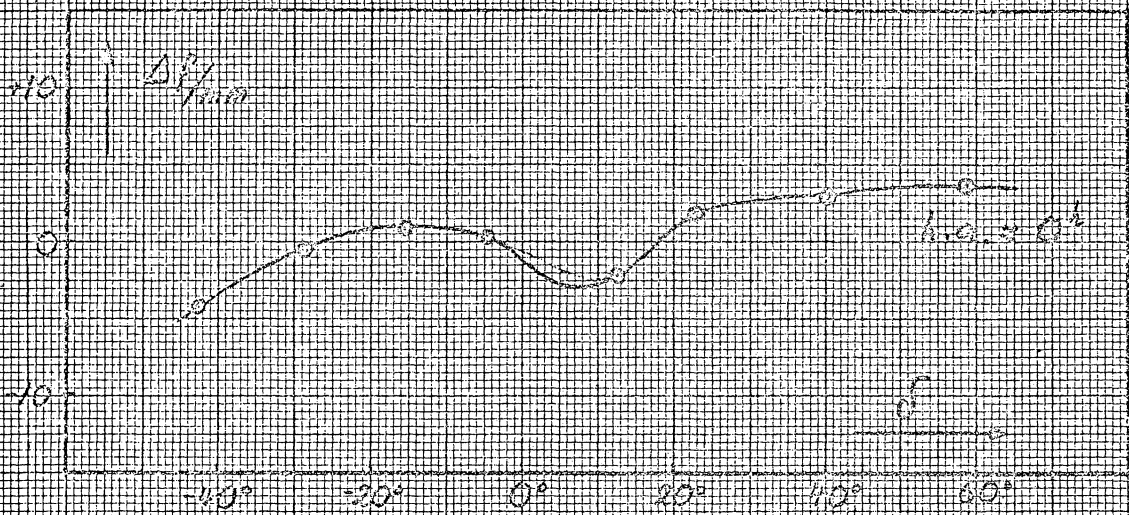
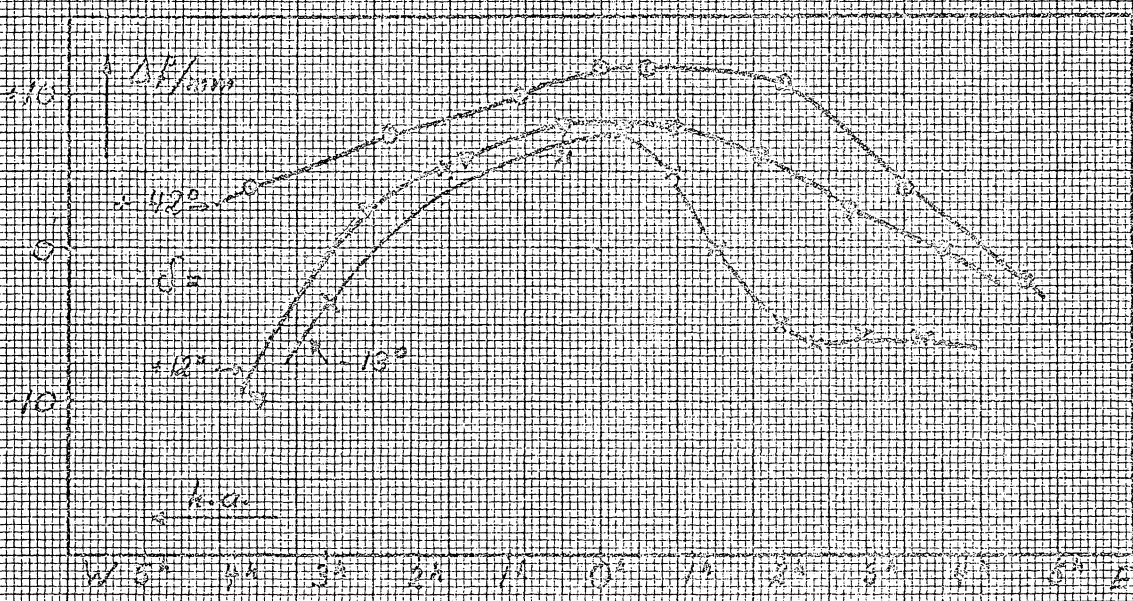


Figure 9b (OP VII)



NRAO 140-foot telescope: Change of focal length as a function of declination. (OPT)



NRAO 140-foot telescope: Change of focal length at three different declinations as a function of hour angle. (OP VII)

Figure 10

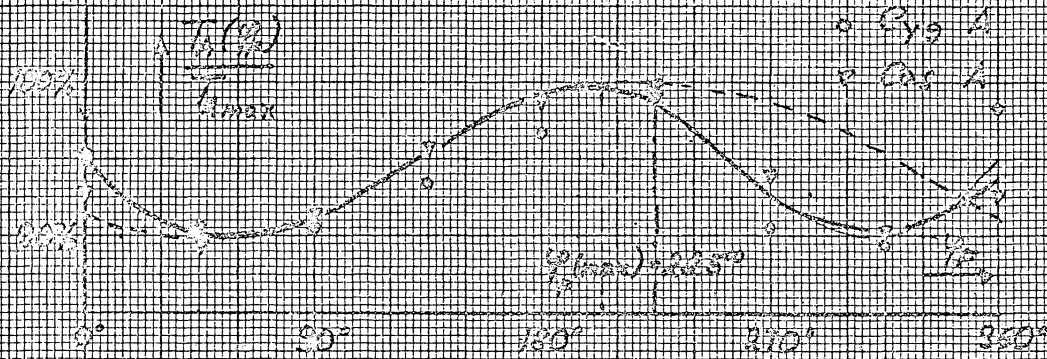
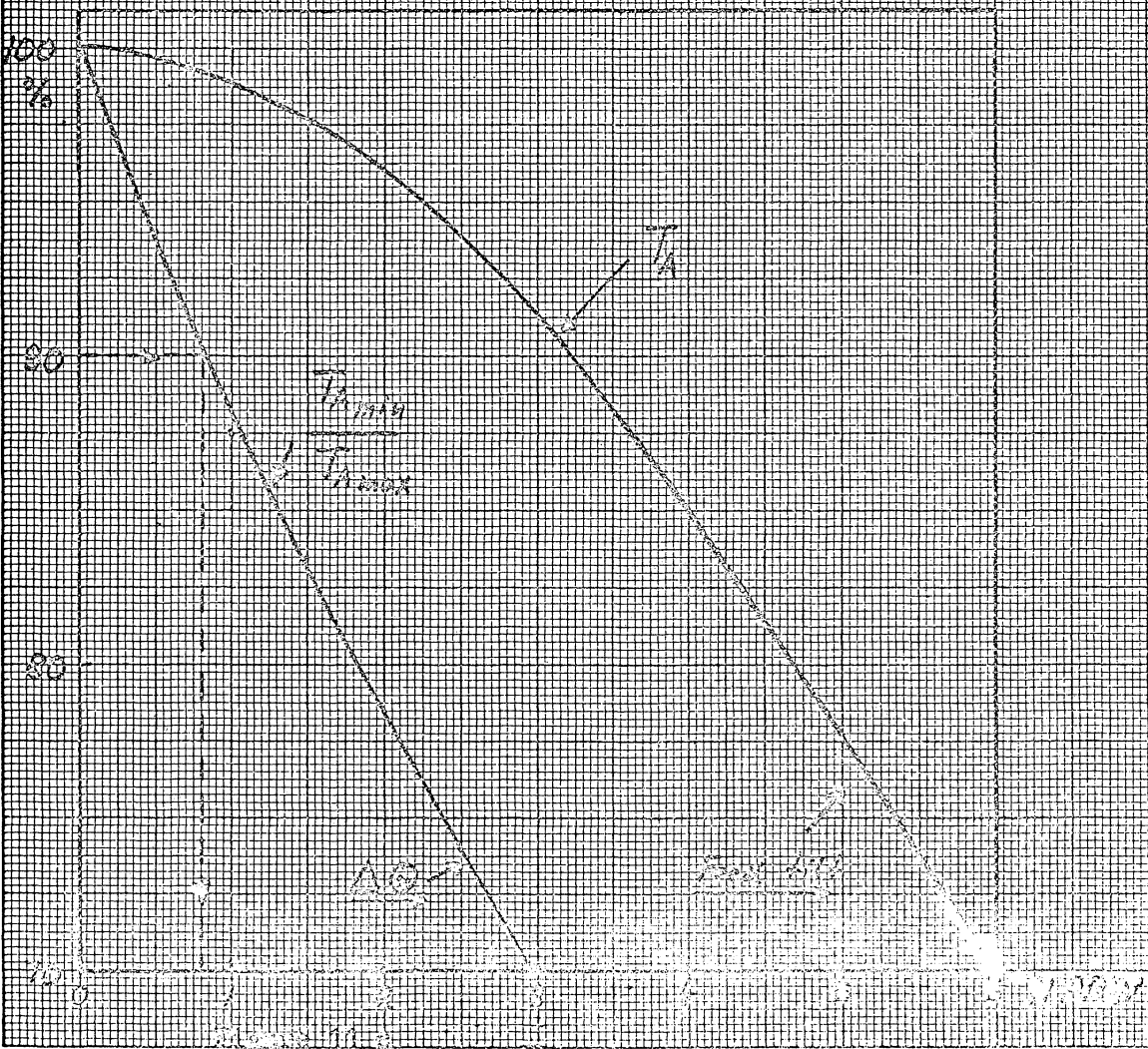
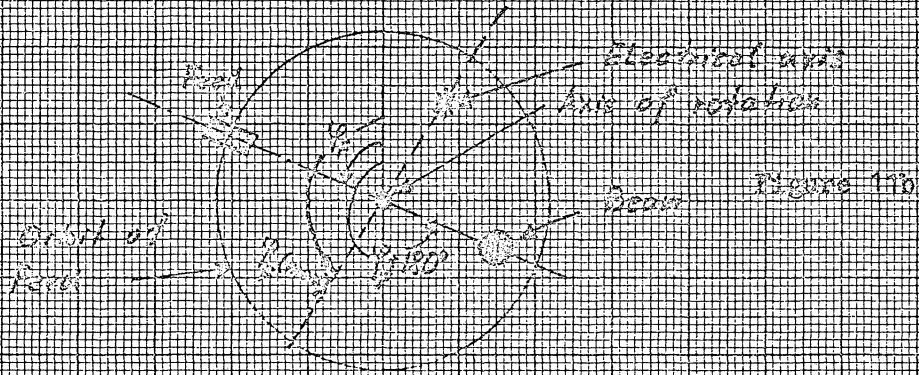


Figure 11a (OPT)



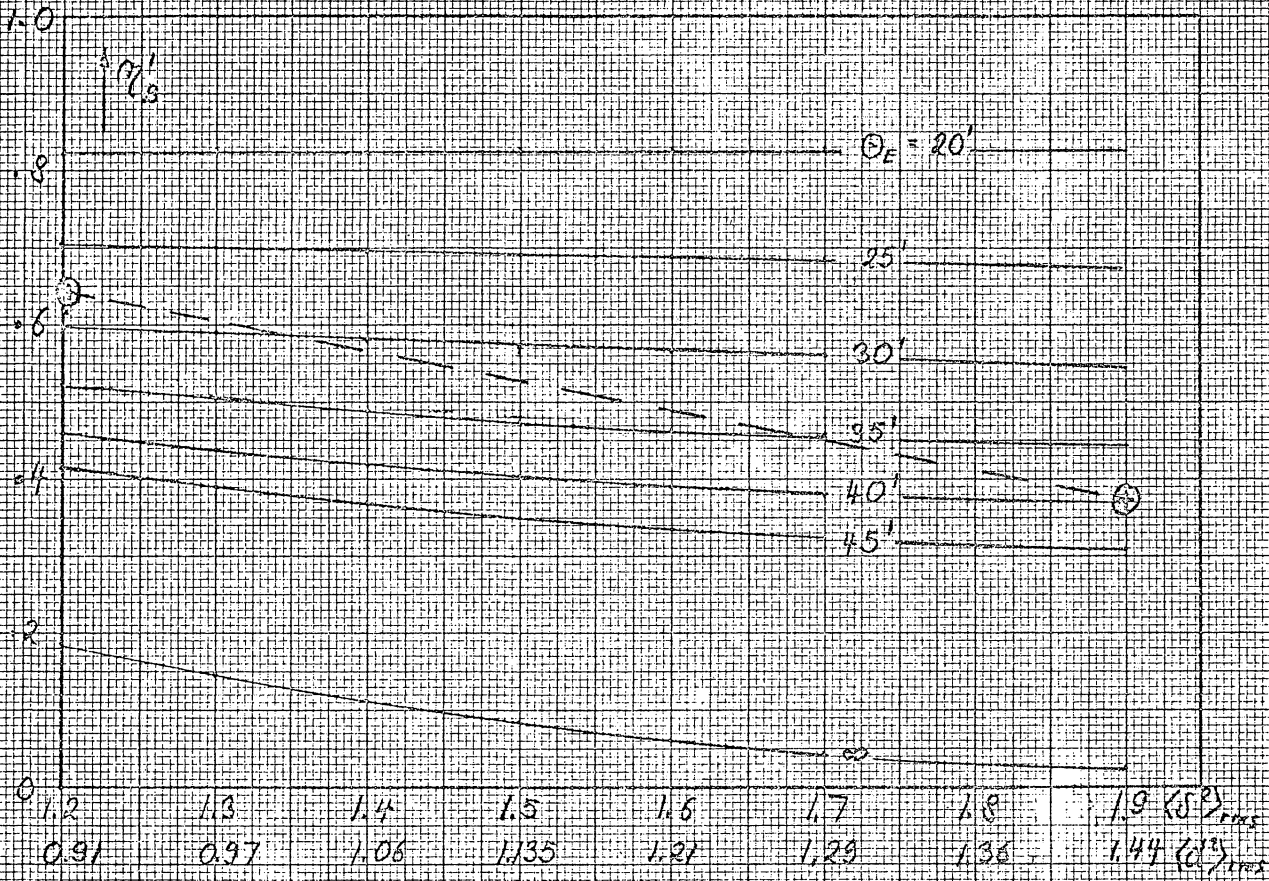


Figure 12b

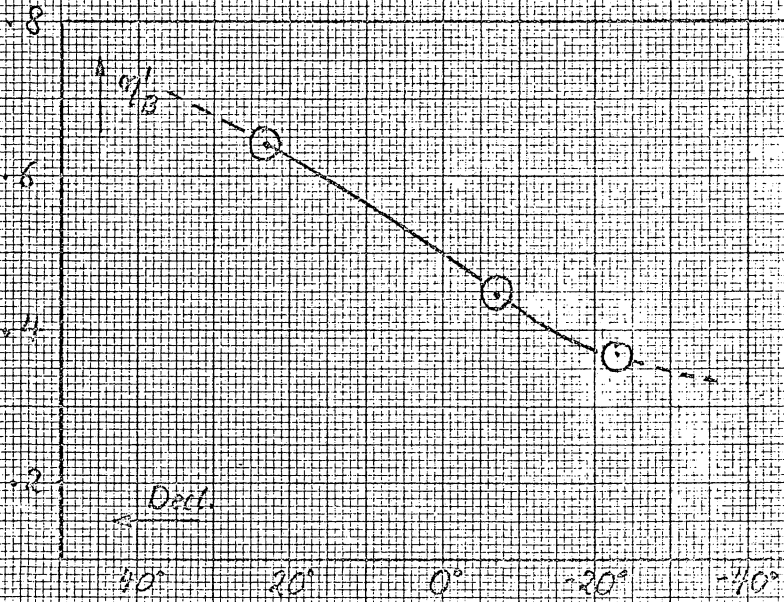


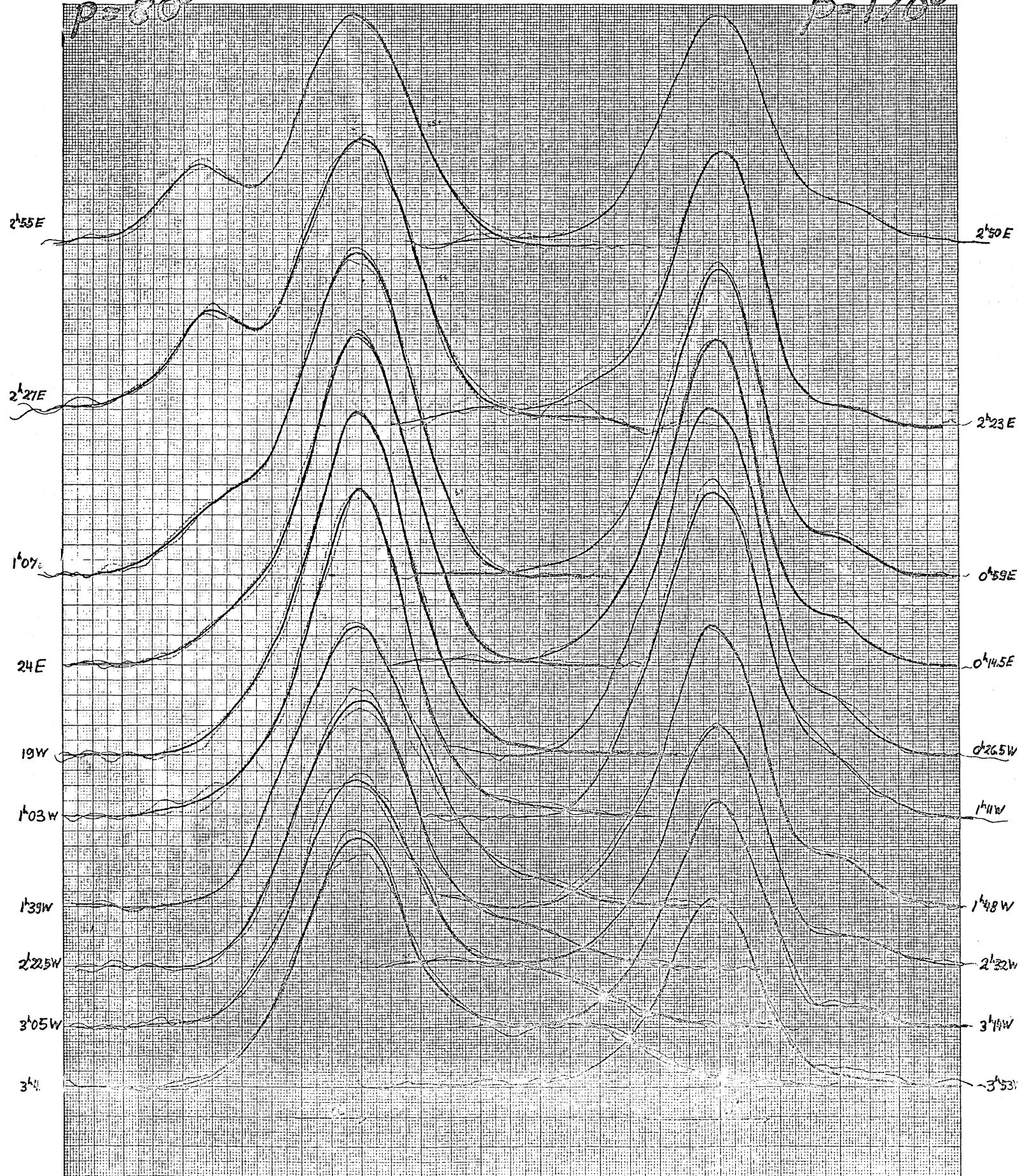
Figure 12a (COPY)

Venus / Test

3-19-66

$p=30^\circ$

$p=170^\circ$



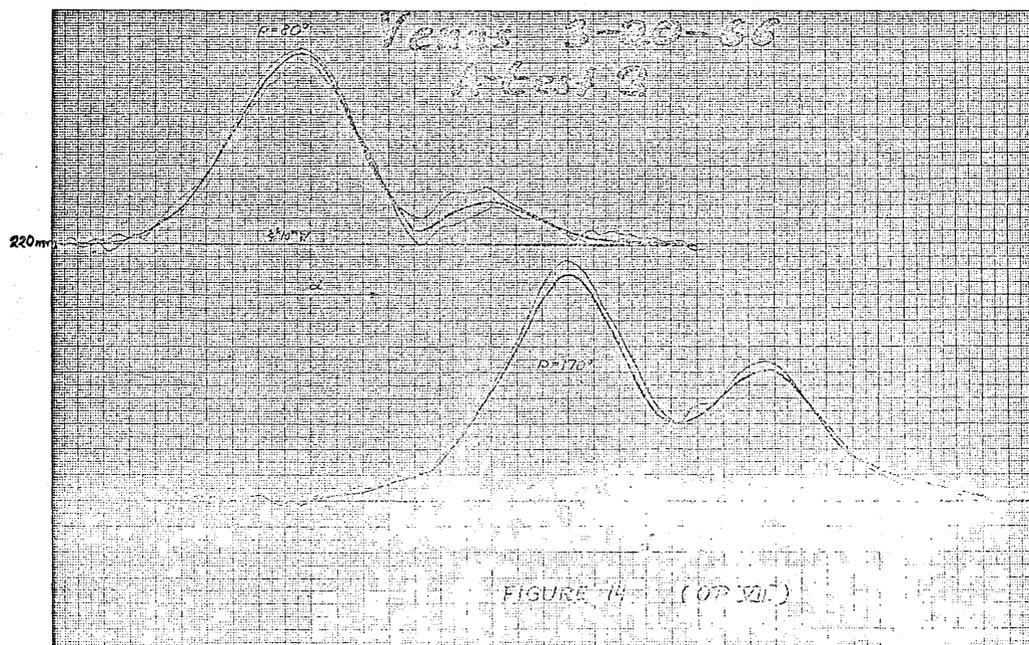
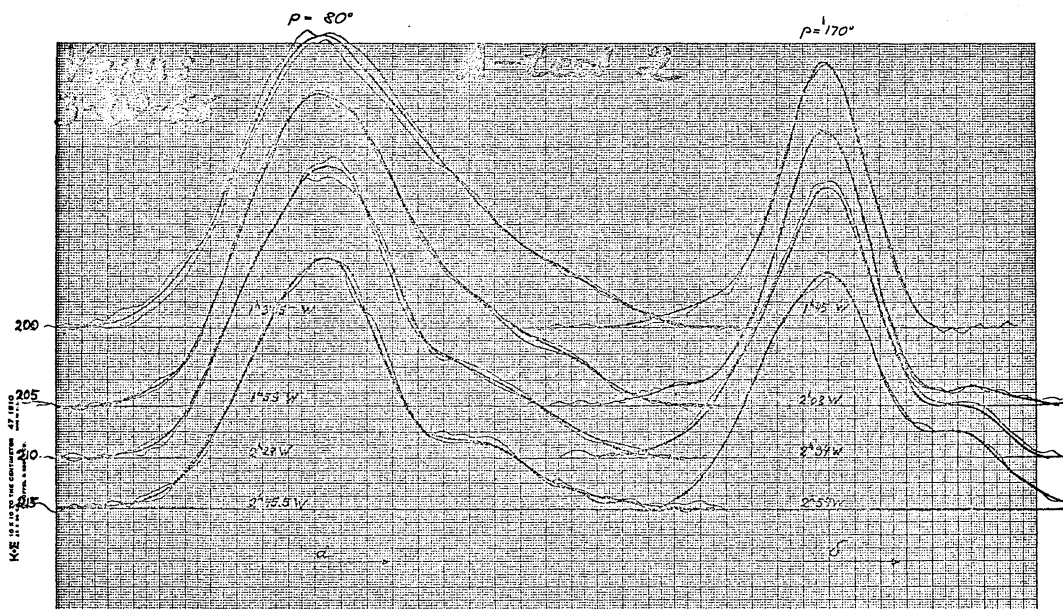
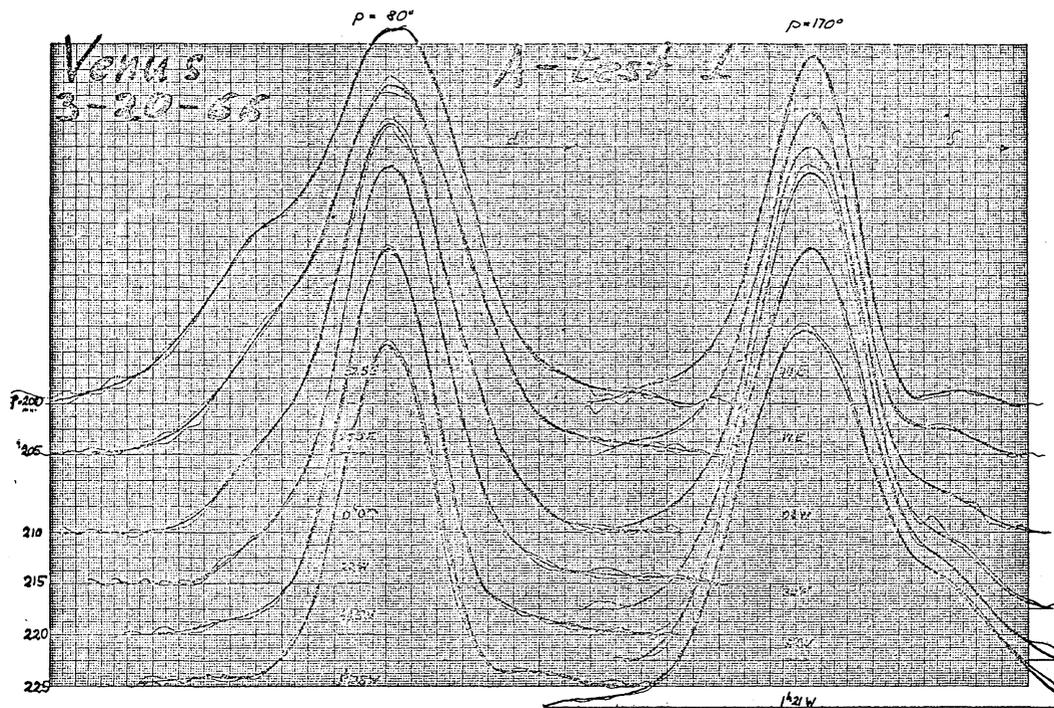


FIGURE 14 (OP 321)

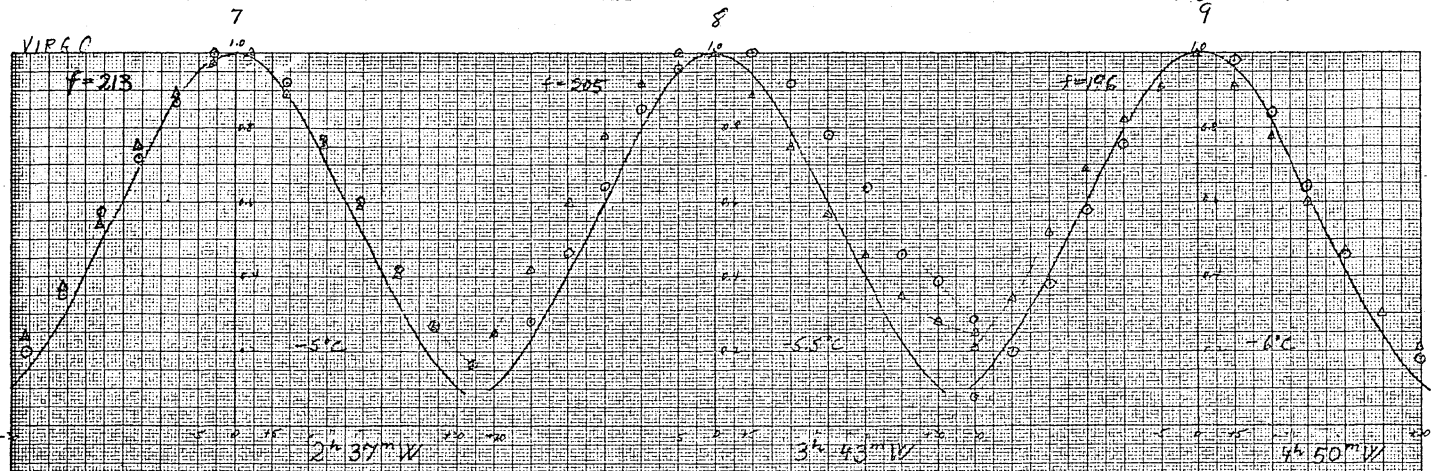
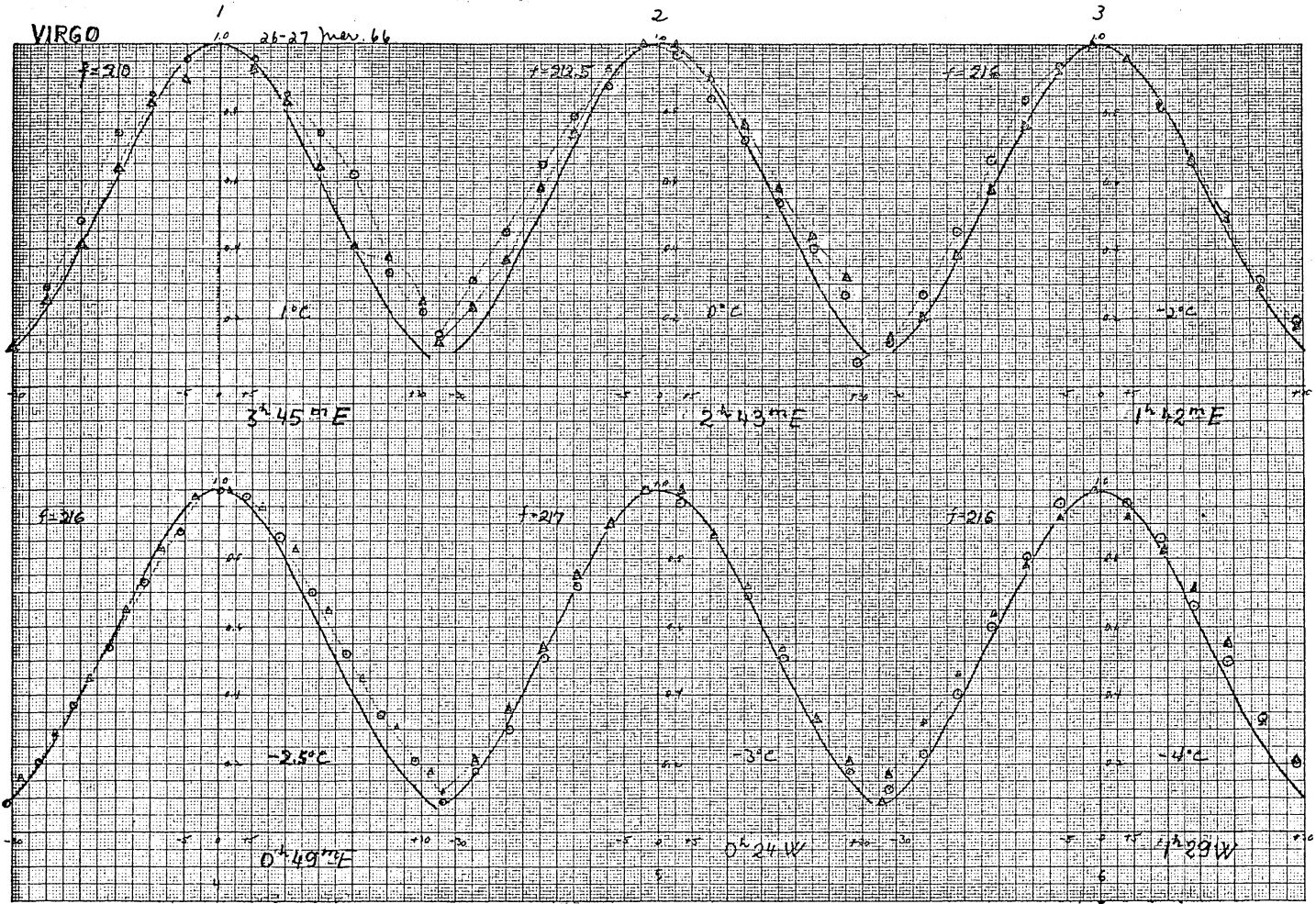


Figure 15a (OP.VII.)

VENUS

1 27 Mar 66

2

3

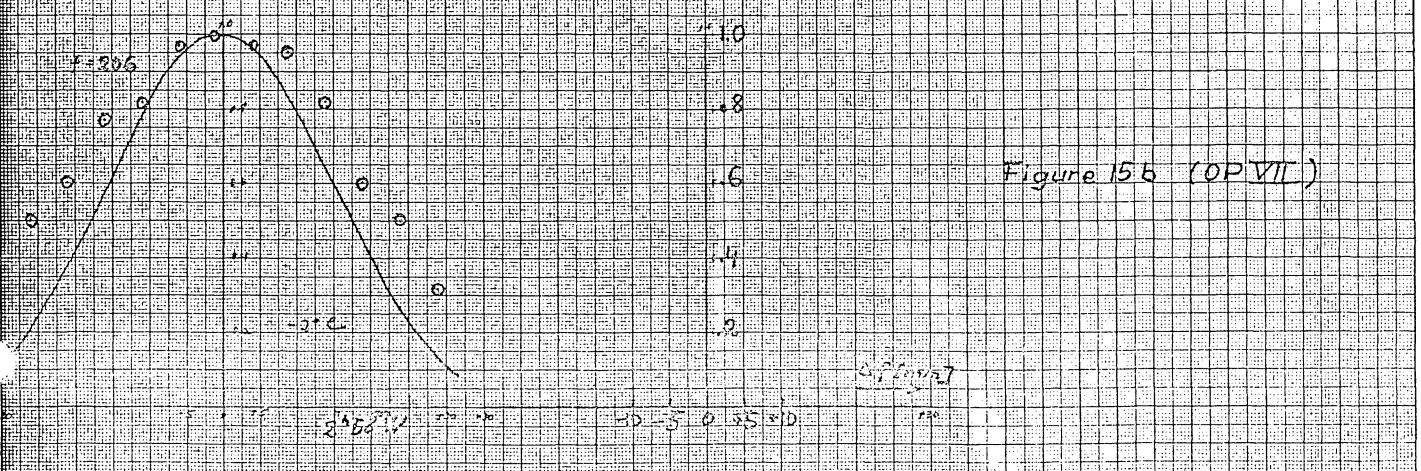
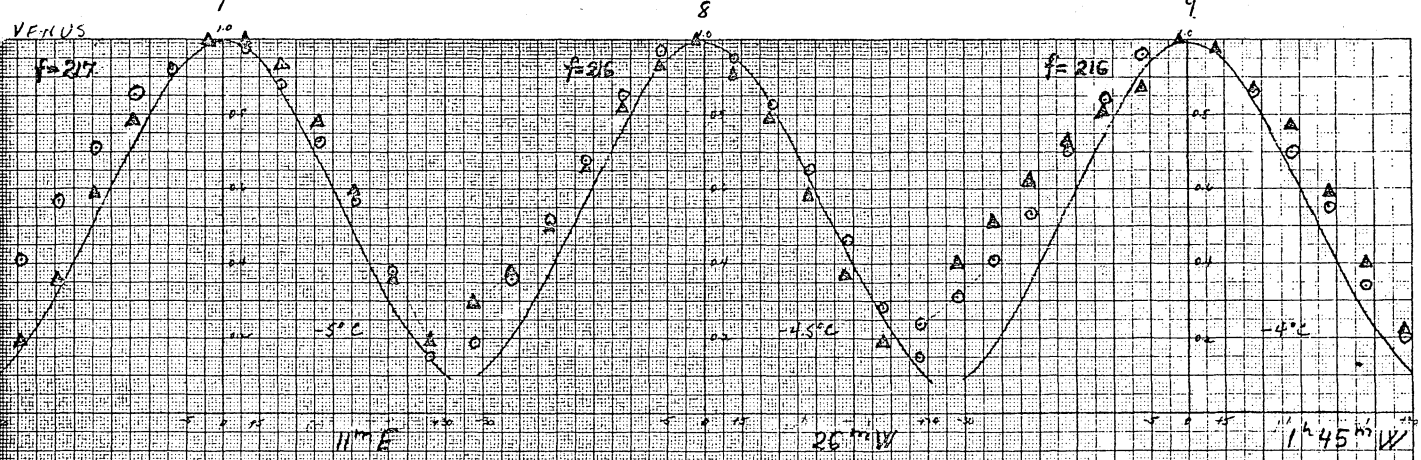
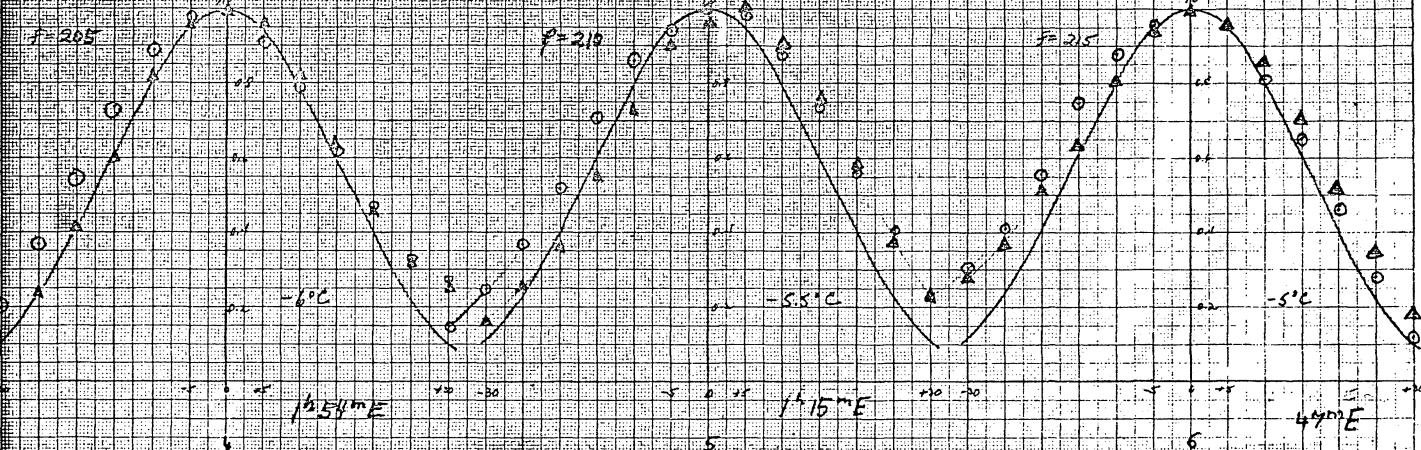
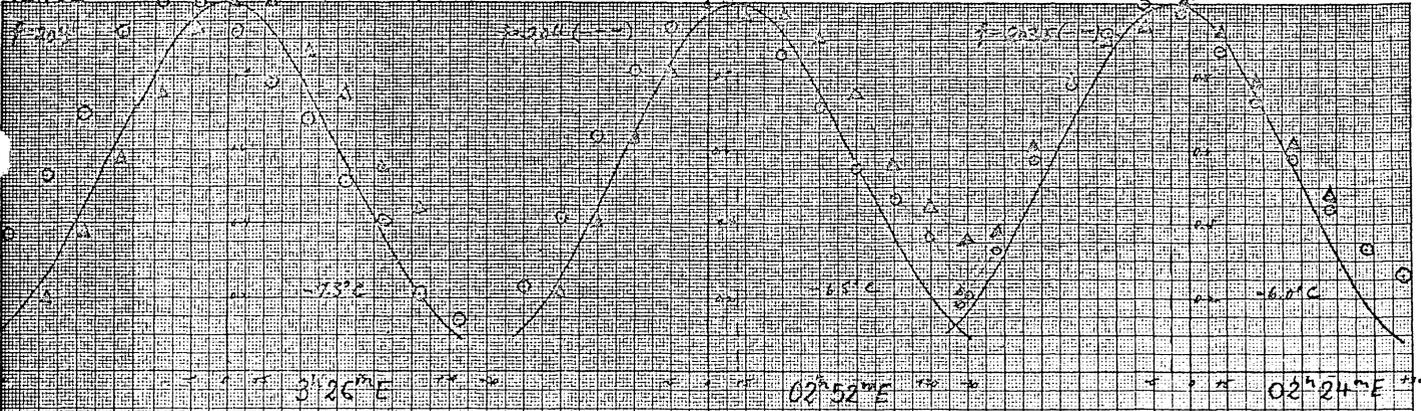
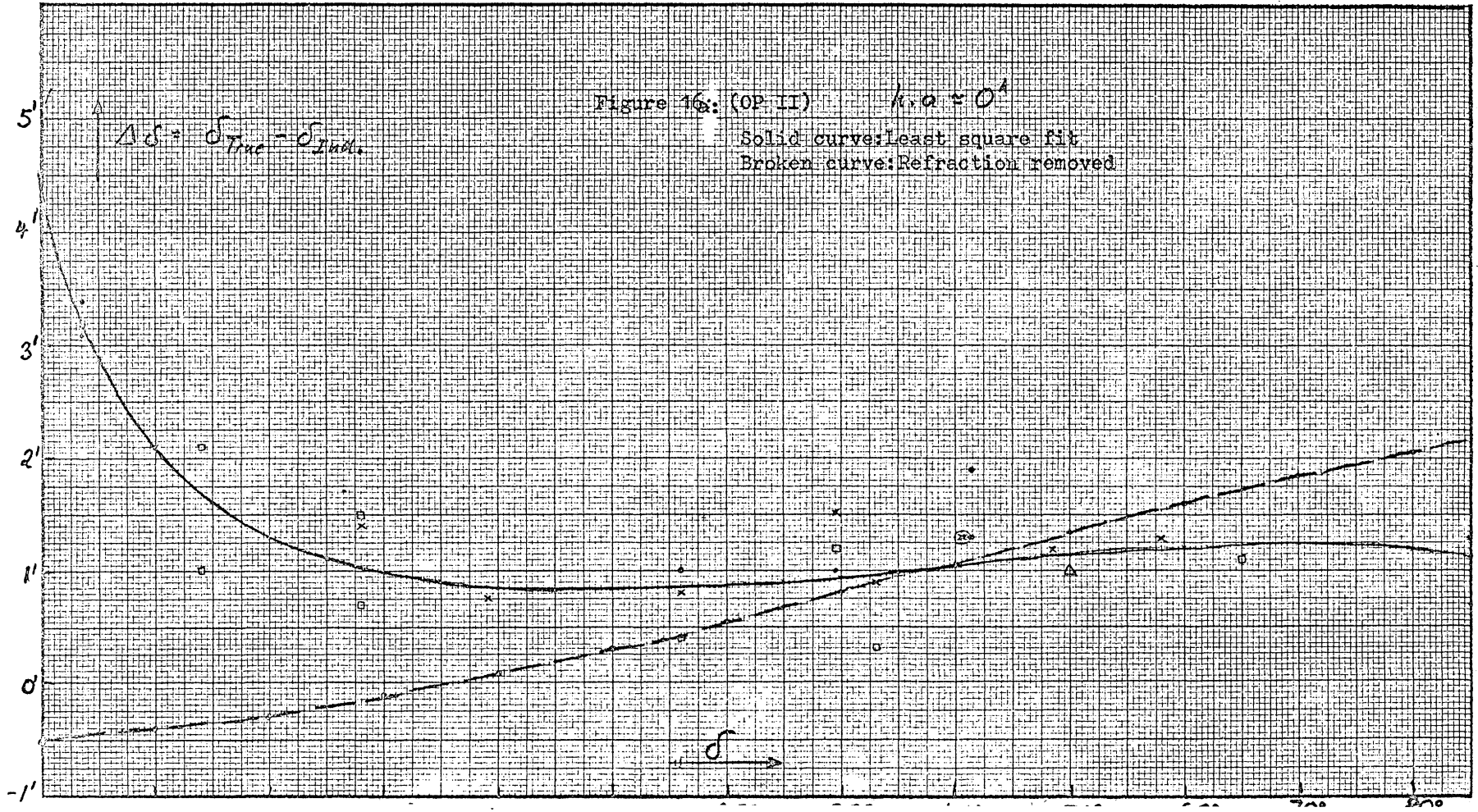
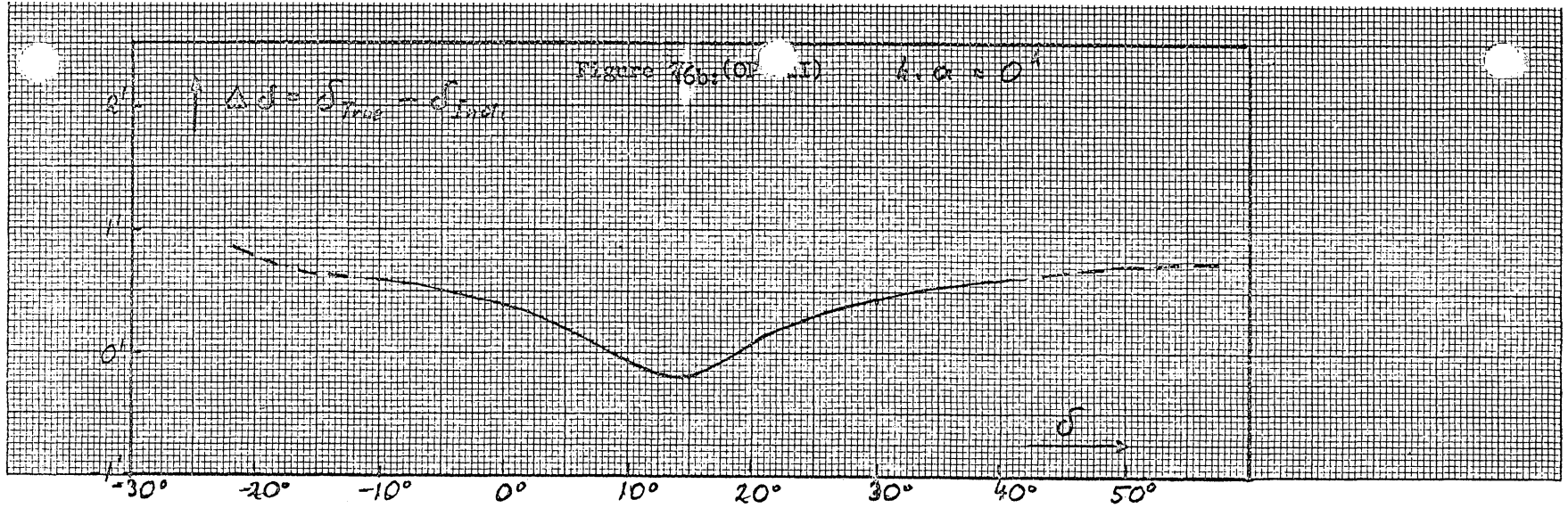
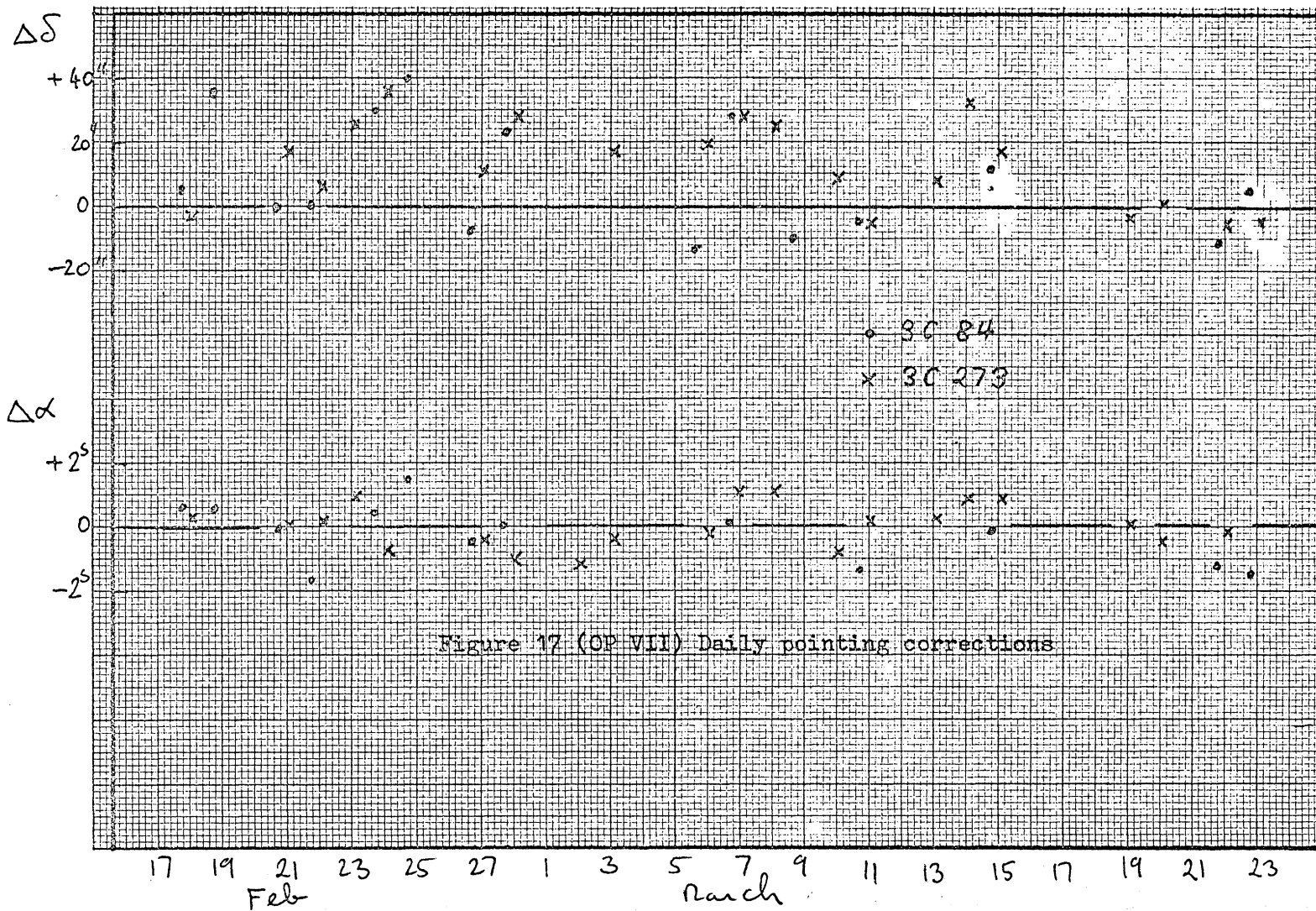


Figure 15b (OP VII)

OP VII

OP VII





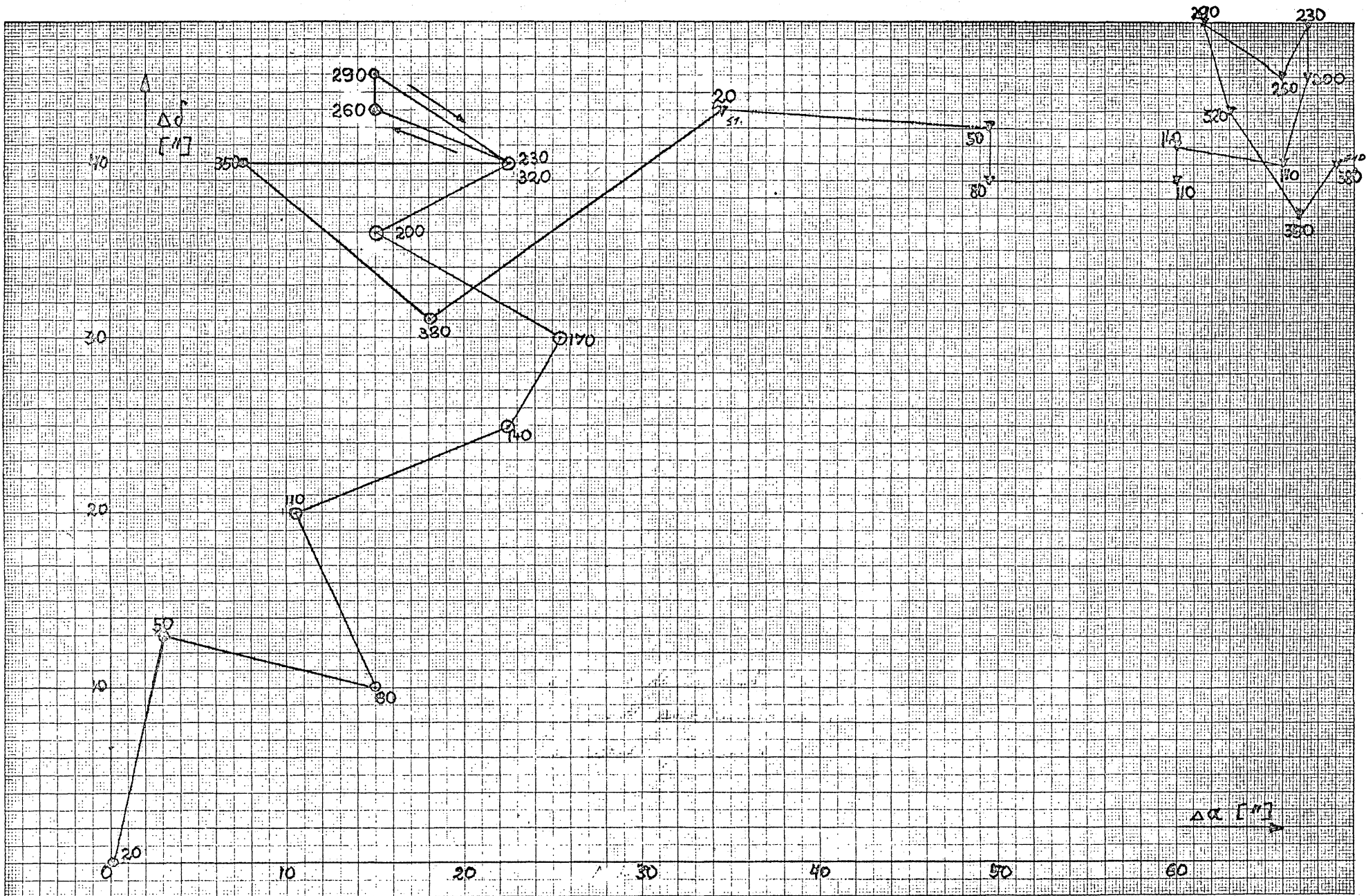


Figure 18 (OP VII)

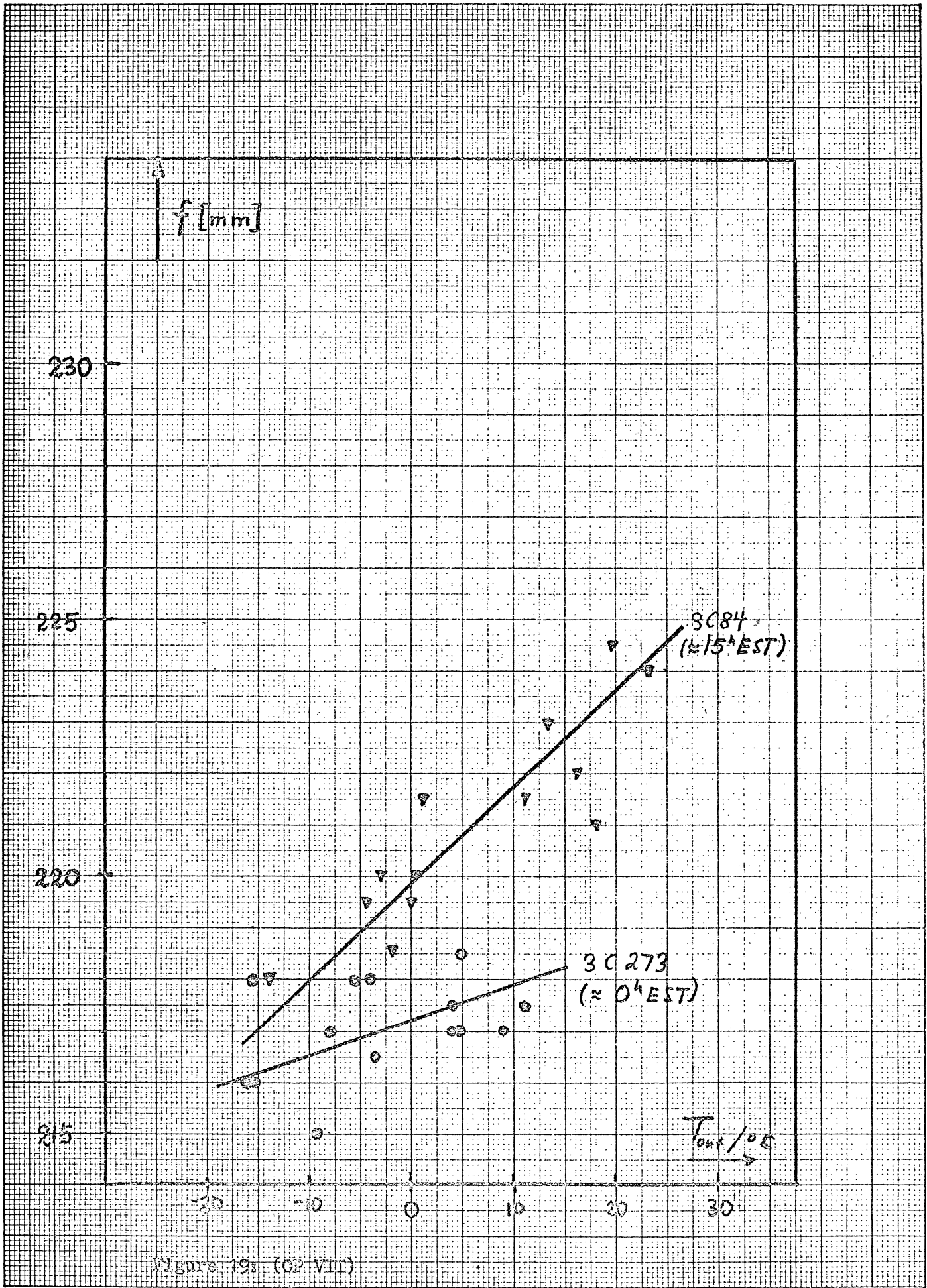


Figure 19: (02 VII)

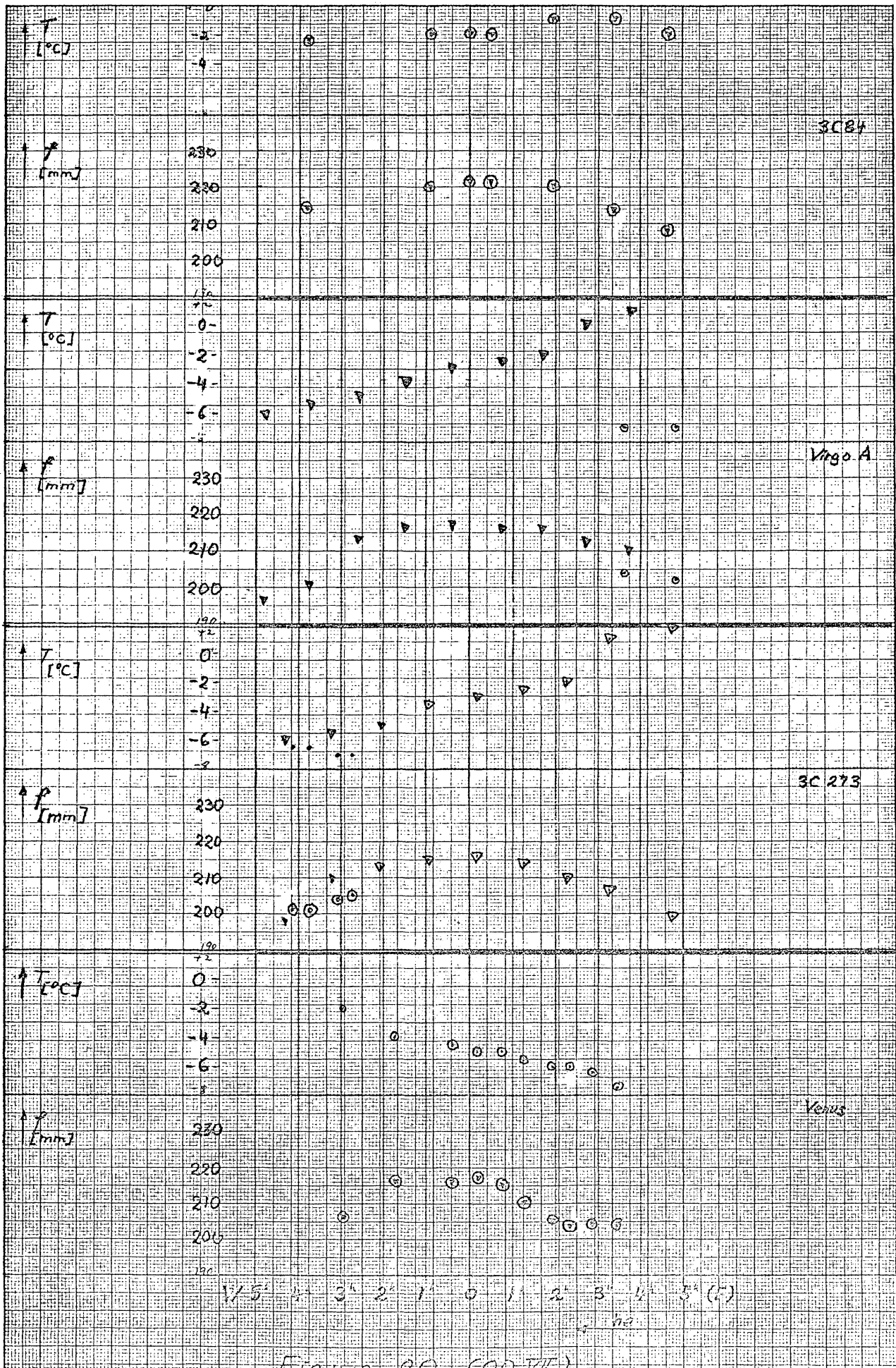


Figure 2A (cont'd)

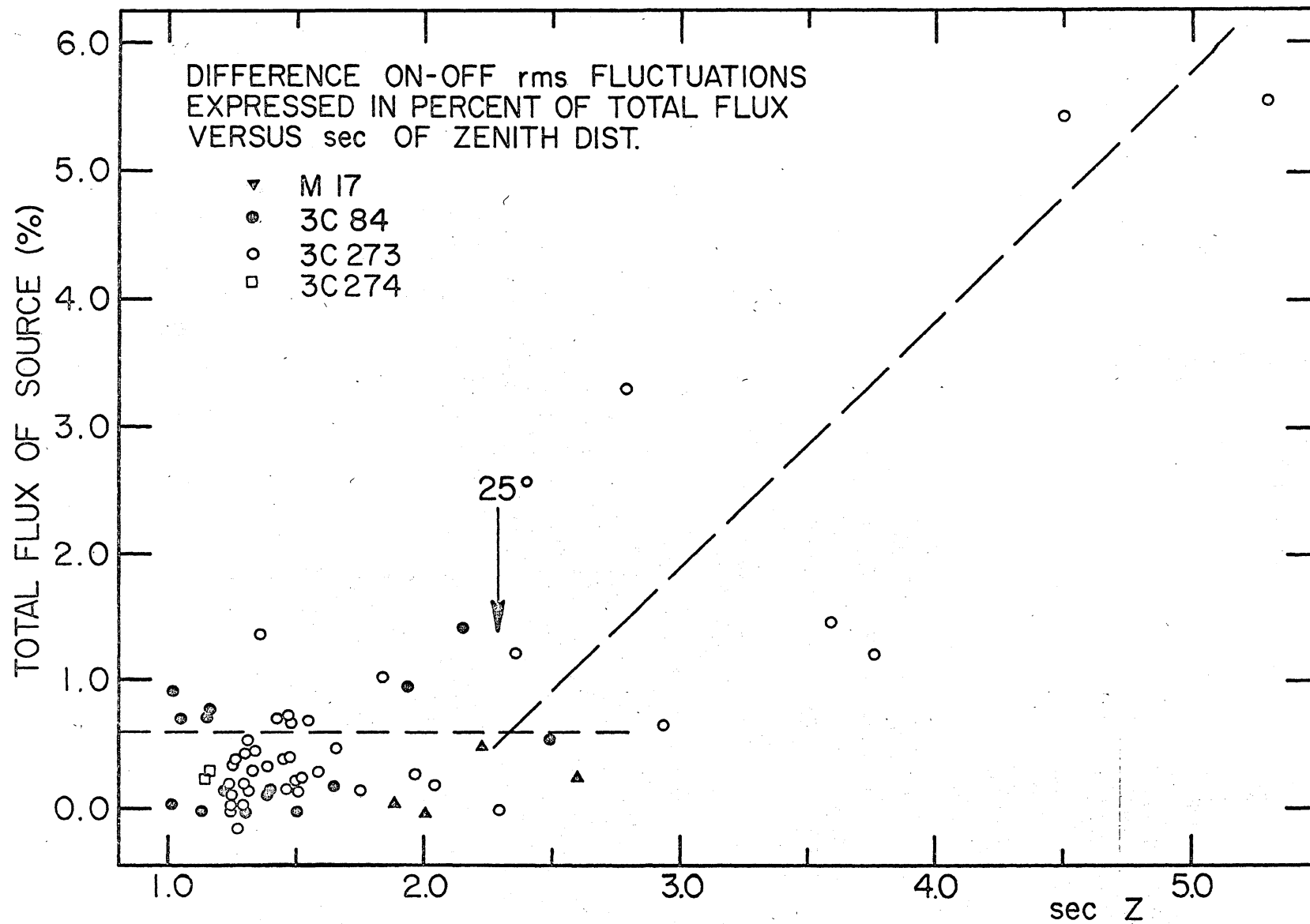


Figure 21

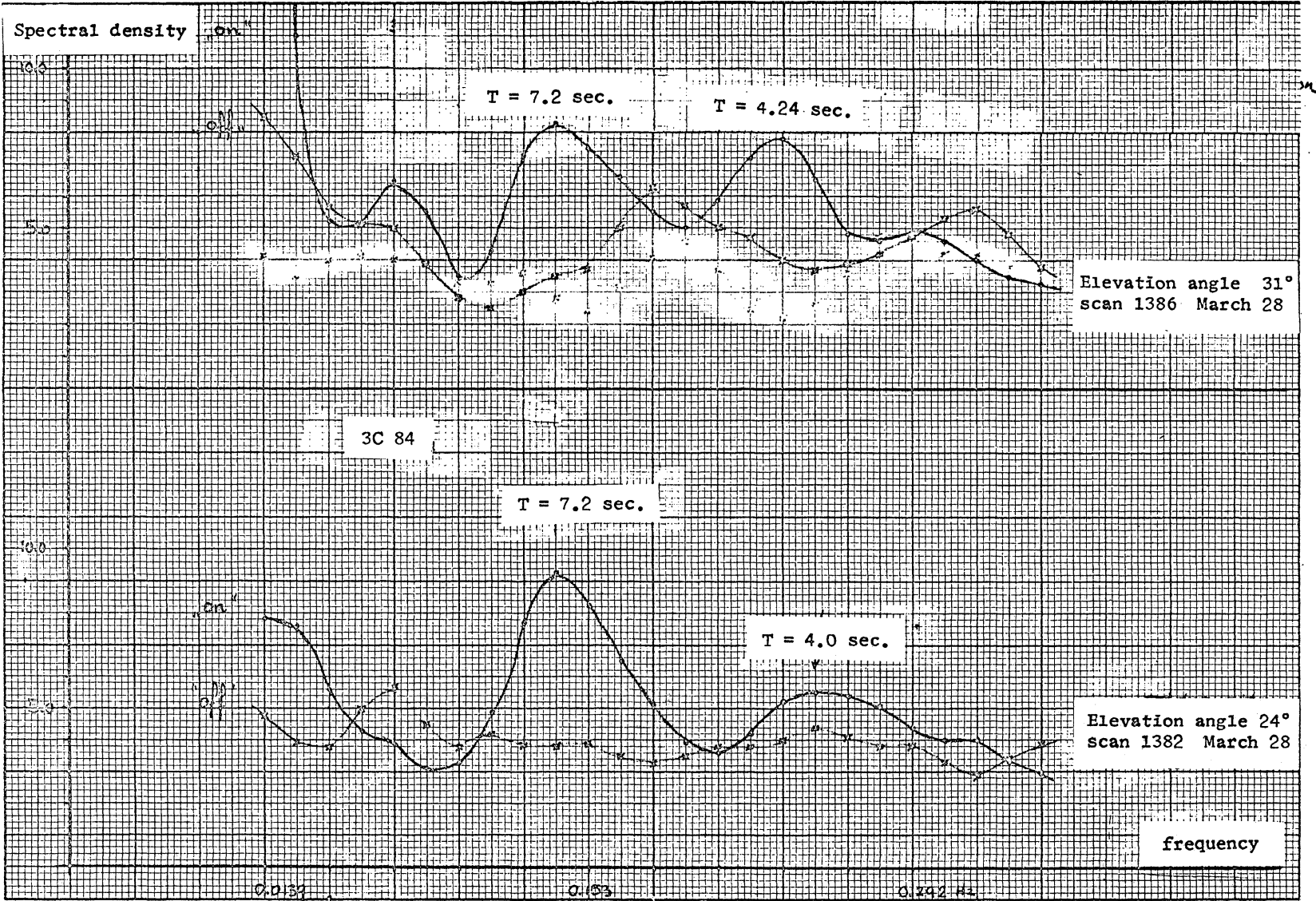


Figure 23